Multi-dimensional modelling of a magnetically stabilized gliding arc plasma in argon and CO_2

Multi-dimensional modelling of a magnetically stabilized gliding arc plasma in argon and CO_2

Hantian Zhang[1,3], Hao Zhang[2], Georgi Trenchev[3], Xiaodong Li[2], Yi Wu[1], Annemie Bogaerts[3]

1 State Key Laboratory of Electrical Insulation and Power Equipment, Xi'an Jiaotong University, 710049 Xi'an, China

2 State Key Laboratory of Clean Energy Utilization, Zhejiang University, 310027 Hangzhou, China

3 Department of Chemistry, Research group PLASMANT, University of Antwerp, Universiteitsplein 1,

B-2610 Antwerp, Belgium

E-mail: wuyic51@mail.xjtu.edu.cn and annemie.bogaerts@uantwerpen.be

Abstract

This study focuses on a magnetically stabilized gliding arc (MGA) plasma. Two fully coupled flow-plasma models (in 3D and 2D) are presented. The 3D model is applied to compare the arc dynamics of the MGA with a traditional gas-driven gliding arc. The 2D model is used for a detailed parametric study on the effect of the external magnetic field. The results show that the relative velocity between the plasma and feed gas is generated due to the Lorentz force, which can increase the plasma-treated gas fraction. The magnetic field also helps to decrease the gas temperature by enhancing heat transfer and to increase the electron number density. This work shows the potential of an external magnetic field to control the gliding arc behavior, for enhanced gas conversion at low gas flow rates.

Keywords: atmospheric pressure plasmas, gliding arc, fluid plasma model, CO_2 conversion, splitting mechanism

1. Introduction

Global climate change due to increasing anthropogenic greenhouse gas emissions is a growing concern. The conversion of greenhouse gases, such as CO_2, into value-added chemicals and renewable fuels is an effective strategy to control greenhouse emissions and to provide hydrocarbon feedstock for the chemical industry. Plasma technology offers unique possibilities for CO_2 decomposition at mild conditions [1]. Different types of plasmas have been used to investigate the CO_2 conversion and energy efficiency. For instance, the influence of discharge power, gas flow rate and Ar dilution on the CO_2 decomposition was studied in a packed-bed plasma [2]. A solar-enhanced microwave plasma was designed to enhance the decomposition of CO_2 at atmospheric pressure [3]. The CO_2 reaction kinetics, especially the vibrational-translational processes in microwave plasma reactors, was studied using a 1D plug flow model [4]. The breakdown and current-voltage characteristics were investigated to explore the possibility of CO_2 decomposition in the micro-slit discharge [5].

Among different kinds of plasmas, a gliding arc (GA) plasma, which presents advantages of both thermal [6] and non-thermal plasmas, has been recognized as one of the most attractive options. Indeed, GA plasmas are capable of reaching promising energy efficiency for CO_2 splitting (around 30%) and dry reforming of methane (around 60%) [1], even when operating at atmospheric pressure. In addition, GA reactors can be built at relatively low cost compared with other types of plasma reactors, showing their potential for large-scale industrial applications in the future.

In the past two decades, different kinds of GA reactors have been proposed and tested. In a classical GA [7,8], two divergent electrodes are used as anode and cathode. The arc plasma is ignited at the shortest gap between the electrodes, and blown downstream under the effect of feed gas flow, so that it elongates and the arc voltage increases to a critical value. Once the elongated arc cannot be sustained anymore, a new arc will ignite at the shortest gap and start a new loop. Based on the classical GA design with two electrodes, also GA reactors with three [9] and six electrodes [10] were developed, to enhance the plasma volume, and hence the fraction of gas that can be treated by the plasma.

Furthermore, in order to achieve longer residence times of the gas in the plasma and to overcome the inhomogeneous gas treatment inherent to the classical GA, rotating gliding arc (RGA) reactors [11] with a conical

inner electrode and hollow outer electrode were proposed. In addition, a reverse vortex flow GA (also called gliding arc plasmatron, GAP) [12,13] was designed to allow a larger fraction of the feed gas being treated.

The dynamic behavior (like elongation or rotation) of the arc plasma in the above GA reactors is mainly dominated by the feed gas flow. The gas flow will cool the arc by strong convection and result in high non-equilibrium. These GA plasmas can be classified as gas-driven gliding arc (GDGA). However, being a conductor, arc plasmas can also be controlled by the Lorentz force, provided by an external magnetic field.

In practice, the external magnetic field is achieved by a stack of permanent magnets, and is usually applied axially to an RGA reactor. In Ref [14], such kind of GA was named as magnetically stabilized gliding arc (MGA). Zhang et al. [15] developed an RGA co-driven by a magnetic field and tangential flow for CO_2 conversion. A CO_2 conversion of around 4% and an energy efficiency of 16-17% could be achieved. Using high-speed imaging and electrical diagnostics, McNall and Coulombe [16] investigated the dynamics of the MGA in argon. In Ref [17], a novel MGA reactor combing a classical GA and external magnetic field was developed, yielding 12.2% CO_2 conversion and 24.3% energy efficiency at 4 L/min.

To improve the performance of the MGA, a better understanding of their behaviors is required, which can be obtained by computer modelling. The mechanisms of CO_2 conversion in GDGA have been studied by several papers [18–21]. However, research work dealing with modelling of an MGA is very limited. The flow field distribution inside an MGA reactor at different gas flow rates was modelled using the Re-Normalization Group k-epsilon model [22]. The arc rotation frequency was calculated in Ref [14,16,22], assuming the Lorentz force and aerodynamic drag force from the surrounding gas were equal. In Ref [23], a zero-dimensional chemical kinetics model was developed to describe an MGA in CH_4/N_2. However, to our knowledge, a fully coupled (2D/3D) flow-plasma model for a MGA has not been developed yet.

Therefore, in this paper, we present for the first time such a fully coupled (2D/3D) flow-plasma model, including the Lorentz force, to obtain a better insight into the effect of an external magnetic field on the GA plasma behavior. We also present experimental results about the dynamic behavior of the MGA, to validate our model. The objective of this work is to reveal the differences between a GDGA and an MGA and how these differences affect the performance (conversion rate and energy efficiency) of a GA plasma for CO_2 conversion.

2. Experimental setup of the MGA reactor

The experiments are used to validate the simulations for the plasma shape, arc length, plasma moving speed and the electron temperature, as will be shown in section 4.1 below. Figure 1 shows the experimental setup. The MGA reactor was developed at Zhejiang University. More details of the reactor can be found in Ref [15,24]. A DC power supply with a voltage of 10 kV (TLP2040, Teslaman) and a 40 kΩ ballast resistor is connected in series with the MGA. The feed gas (Ar or CO_2) passes through a mass flow controller (YJ-700C, Sevenstar) and is injected tangentially into the bottom of the reactor. It generates a swirling and upward moving flow (see blue solid line) inside the reactor. The ring permanent magnets outside the cylindrical cathode produce an axial magnetic field (see black dashed lines). The flux density of the external magnetic field is about 0.2 T at room temperature. The operating temperature of the magnets will increase when the power supply is turned on, so the magnetic flux density decreases. The arc is first ignited near the gas inlet, at the shortest distance between the cathode and cone-shaped anode. Subsequently, it is pushed upwards by the feed gas. A mirror is placed at the end of the MGA reactor to reflect the images of the MGA plasma into the lens of a digital high-speed camera (V2512, Phantom). The exposure time and sample rate of the high-speed camera are 25 μs and 39,000 frames per second, respectively. The arc voltage and arc current are recorded by an oscilloscope (Tektronix DPO4034B) using a high-voltage probe and a current sensor.

The Saha-Boltzmann plot method [25] was used to measure the excitation temperature of the MGA in Ar. The excitation temperature can be assumed equal to the electron temperature [26]. 7 Ar I lines and 4 Ar II lines from 357.66 nm to 738.40 nm [27] were used in this experiment. The light emitted from the gliding arc was collected and transmitted to a spectrometer (SP2750, Acton) with 0.75 m focal length and an intensified CCD camera (ICCD, PI-MAX2).

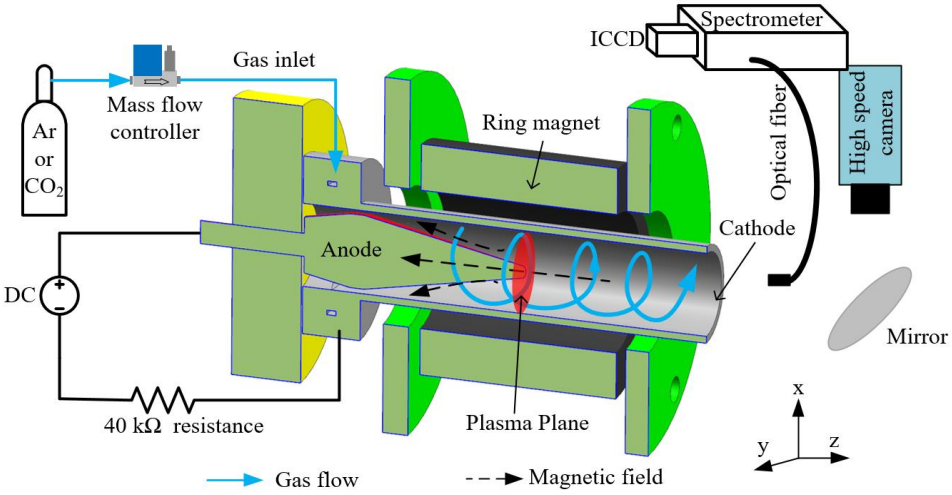

Figure 1: Schematic of the experimental setup, with detailed view of the MGA reactor

3. Description of the model

In our previous 2D/3D models for either classical or cylindrical GA plasmas or other plasma types, like atmospheric pressure glow discharge [19,28–32], we always calculated the gas flow distribution separately by the Navier-Stokes equations, and subsequently, we used it as stationary input data in the plasma model. That is indeed a reasonable approach for GDGAs. However, obviously, the velocity of an MGA plasma is different from the velocity of the surrounding gas. Indeed, experimental results showed that the MGA can rotate quickly at a very low feed gas flow [33] or even without feed gas flow [17]. The gas flow distribution varies with time and cannot be solved in advance, separately from describing the plasma behaviour. Therefore, a fully coupled gas flow-plasma model, in which the Navier-Stokes equations are solved together with the plasma equations, is needed. Such a fully coupled model needs extensive computer memory and calculation time, i.e., above three times more than for the above mentioned separated models.

The dynamic behaviour of the MGA is quite complex. In order to obtain a solution with reasonable computing resources, it is necessary to make some simplifications. Therefore, we don't take the effect of the swirling feed gas flow on the MGA into account in this paper. This is justified for a MGA operating at low flow rate. The effect of the external magnetic field on the plasma behavior will dominate at low gas flow rate, according to the experimental results shown below (Sec.4.1) and in our previous work [22,33]. The MGA also has a longer reaction time at low gas flow rate, which is favorable for achieving high gas conversion [17]. Note that the residence time decreases and the MGA approaches a GDGA upon increasing gas flow rate, and the turbulent effect due to high gas flow rate can then be more important than the external magnetic field. Moreover, the coupled simulation of turbulent gas flow and plasma needs a much finer mesh and thus more calculation time. Therefore, we only focus here on the effect of the external magnetic field on the plasma behavior at low gas flow rates (up to 6 L/min).

We developed two different models in this work. They are both developed using the commercial software COMSOL Multiphysics (version 5.4) [34].The first model is a three-dimensional model (hereinafter called 3D-MGA model) in argon. Under the combined effect of the Lorentz force and swirling gas flow [24], the MGA is anchored at the anode tip and will rotate steadily. A 'plasma plane' is thus generated by the rapid and periodic rotation of the arc, as shown in red in Figure 1. The whole plasma domain has a circular shape with a thickness of a few millimeters. In the 3D-MGA model, we describe only half of this plasma domain to reduce the number of mesh elements needed, instead of the entire circle. The geometry considered in the 3D-MGA model is shown in Figure 2(a). The axis of the cylindrical cathode and cone-shape anode is located at x = y = 0 mm (i.e., center of Figure 2(a)). The diameter of the cylindrical cathode is 20 mm, based on the experiment. The cone-shape anode is simplified as a cylinder with diameter of 3 mm. Without the aerodynamic drag force in the axial direction of the reactor, the arc does not bend in the 'z' direction of Figure 2 (a). With such simplification, we can assume a symmetry plane (z = 0 mm, indicated in purple in Figure 2) perpendicular to the z-axis. Therefore, we only need to model 1/4 of the domain (indicated in gray in Figure 2) in our 3D-MGA model. This significantly reduces the calculation time. Nevertheless, we still need to use about 540,000 tetrahedral mesh elements.

In order to start the calculation, the arc is ignited at the position shown in red in Figure 2(a). The arc current I is obtained by surface integration of the current density over the cathode $I = \int_S Jds$. The cathode is connected to the ground. The anode potential V_{Anode} is the arc voltage and is derived from the external electrical circuit equation (following Ohm's law): $V_{PowerSource} = V_{Anode} + I \bullet R_{Ballast}$ [29,35].

The second model is a two-dimensional cross-section model (2D-CS model) developed for CO_2. As will be discussed in Sec.4.2, the spatial structure of the MGA is quite different from traditional GA plasmas, which are only driven by the high-speed feed gas flow. In previous 2D models [28,35], the arc currents were parallel to the modelling plane. The simulated arc was a 'slab' with infinite depth in the direction perpendicular to the simulation plane. Such an approximation, however, would lead to incorrect pressure distribution for an MGA. Hence, the previous '2D arc' models would not allow to accurately describe the MGA. On the other hand, a fully coupled 3D-MGA model (i.e., our first model) is already very time-consuming for argon. Therefore, applying such 3D modelling for the MGA in CO_2 gas, which contains more chemical species, would currently be impossible. Therefore, we developed a simplified model (2D-CS model) to describe the CO_2 plasma, and we also apply the latter model for argon, in order to be able to compare the results of the 3D-MGA and 2D-CS model. The calculation time can be significantly reduced by choosing the modelling domain to be perpendicular to the arc current [36]. This model is very valuable for parametric studies of the GA behavior. In the 2D-CS model, the arc ignition is achieved by inducing an artificial heating term, which is centered at y = 1 mm, x = 0 mm (see red half circle in Figures 2(b)) [29]. For the argon plasma, we use the same chemistry set and governing equations in the 3D-MGA and 2D-CS model. The only difference is that the current density in the 2D-CS model is defined based on the fact that $J \propto \sigma$ and with a fixed arc current $I_{tot} = \int Jds$, instead of solving the electric potential equation and the electrical circuit equation, as in the 3D-MGA model. In the experiment, the current changes with time, but it varies only slightly around a certain value. This value is mainly related to the voltage of the power supply and the ballast resistor, for example, 230 mA [24]. Therefore, we assumed a fixed arc current in the 2D-CS model for simplification. In our 3D-MGA model, we used the external electrical circuit equation to obtain the arc current, which is closer to the experimental conditions. The arc current flows along the x-axis, while the external magnetic field is applied in the negative z-direction (see Figure 2(b)). Therefore, the GA moves downward under the Lorentz force.

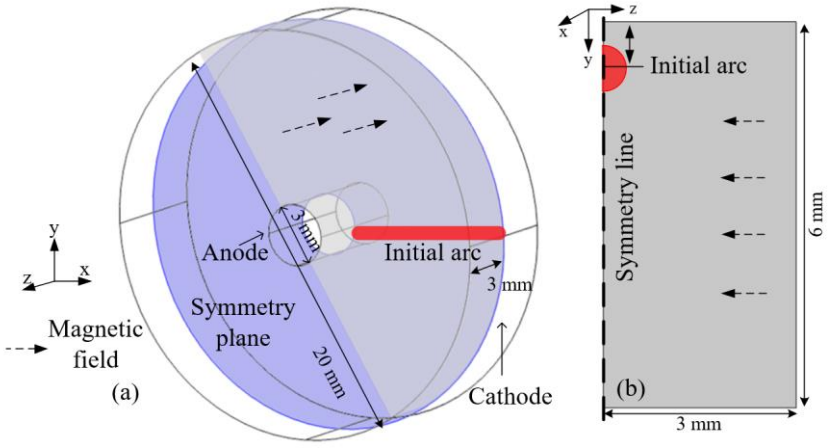

Figure 2: Geometries considered in the model (in gray): (a) 3D rotating (3D-MGA) model and (b) 2D cross-section (2D-CS) model. The position where the arc is ignited is indicated in red.

The governing equations of the fully coupled gas flow-plasma quasi-neutral model are as follows. The species number densities are solved by the species continuity equation:

$$\frac{\partial n_s}{\partial t} + (\vec{u} \bullet \vec{\nabla}) n_s + \vec{\nabla} \bullet \vec{G}_s = S_s \tag{1}$$

where n_s is the number density of species 's', $\vec{u}$ is the gas velocity. S_s is the net source term, representing the number of species per volume and time produced or lost due to chemical reactions. $\vec{G}_s$ is the species flux, which can be expressed with the drift-diffusion approximation:

$$\vec{G}_s = -D_s \nabla n_s + \frac{q_s}{|q_s|} \mu_s n_s \vec{E}_{amb} \tag{2}$$

where μ_s is the species mobility, D_s is the diffusion coefficient, q_s is the charge of species '*s*', and $\vec{E}_{amb} = \frac{\sum_s \frac{q_s}{|q_s|} D_s \nabla n_s}{\sum_s n_s \mu_s}$ is the ambipolar electric field. Only charged particles, like ions and electrons, contribute to $\vec{E}_{amb}$. For neutral species the flux is only governed by diffusion, $\vec{G}_s = -D_s \nabla n_s$.

The electron energy equation is as follows:

$$\frac{\partial n_e \bar{\varepsilon}_e}{\partial t} + (\vec{u} \bullet \vec{\nabla}) n_e \bar{\varepsilon}_e + \vec{\nabla} \bullet \vec{G}_{\varepsilon,s} = \sigma \vec{E}^2 - Q_{ecoll} + Q_{ini} \tag{3}$$

where $\bar{\varepsilon}_e$ is the average electron energy. The first term on the right-hand side is the Joule heating term. σ is the electric conductivity and $\vec{E}$ is the electric field. In the 3D-MGA model, the electric field is calculated by solving the Laplace equation for electrostatics (electric potential equation) $\nabla^2 \varphi = 0$, $\vec{E} = -\nabla \varphi$, where φ is the electrical potential. In the 2D-CS model, the electric field is calculated from the current density $\vec{E} = \vec{J} / \sigma$.

The second term on the right-hand side is expressed as:

$$Q_{ecoll} = \sum_j \frac{3 k_B m_e m_j (T_e - T_j)}{(m_e + m_j)^2} n_e n_j k_j + \sum_i \Delta H_i R_i \tag{4}$$

It represents the energy transfer of electrons due to elastic and inelastic collisions (first and second term in equation (4)), where k_B is the Boltzmann constant, $T_e = (2/3)\bar{\varepsilon}_e$ is the electron temperature, m_j is the mass of species *j*, k_j is the elastic collision rate coefficient, and ΔH_i and $R_i = k_i \prod_l n_l$ are the energy loss and reaction rate of reaction *i, with* k_i being the rate coefficient.

The last term on the right-hand side of equation (3), Q_{ini}, is the artificial heating term to ignite the arc, which has a Gaussian function over space and a triangular function over time [29].

Equation (3) also contains the electron energy density flux, $\vec{G}_{\varepsilon,s}$, which is expressed by:

$$\vec{G}_{\varepsilon,s} = -D_{\varepsilon,e} \nabla (n_e \bar{\varepsilon}) - \mu_{\varepsilon,e} (n_e \bar{\varepsilon}) \vec{E}_{amb} \tag{5}$$

where $\mu_{\varepsilon,e}$ is the electron energy mobility and $D_{\varepsilon,e} = \frac{2}{3} \bar{\varepsilon}_e \mu_{\varepsilon,e}$ is the electron energy diffusion coefficient. More details about the plasma model are available in our previous work [19,28,31,32].

The Navier-Stokes equations are solved together with the species density equations.

$$\frac{\partial \rho}{\partial t} + \vec{\nabla} \bullet (\rho \vec{u}) = 0 \tag{6}$$

$$\rho \frac{\partial \vec{u}}{\partial t} + \vec{\nabla} \bullet (\rho \vec{u} \bullet \vec{u}) = \vec{\nabla} \bullet [-p\vec{I} + \vec{K}] + \vec{F}_{Lor} \tag{7}$$

where ρ is the gas density, which is the sum of the mass densities of all species, and p is the pressure. The Lorentz force $\vec{F}_{Lor} = \vec{J} \times \vec{B}_E$ is added into the momentum equation as source term.

The energy conservation equation is given by:

$$\rho C_p \frac{\partial T_g}{\partial t} + \rho C_p \vec{u} \bullet \vec{\nabla} T_g - \vec{\nabla} \bullet (k_g \vec{\nabla} T_g) = Q_{hcoll} \tag{8}$$

where C_p is the heat capacity at constant pressure, k_g is the thermal conductivity, Q_{hcoll} is the energy transferred to the heavy particles by elastic and inelastic collisions.

Zero species fluxes and electron energy flux are set for all boundaries. The anode and cathode in the 3D-MGA model follow the 'no slip' boundary conditions, as explained in [19]. A gas outlet boundary condition (pressure equal to atmospheric pressure) for the other boundaries is used, except at the symmetry plane/line. For the electric potential equation in the 3D-MGA model, the electrodes follow the dirichlet boundary conditions, i.e., V_{Anode} for anode and 0 V for cathode.

For the 3D-MGA and 2D-CS model in argon, only five important species are considered, i.e., the electrons, Ar ground state atoms, Ar(4s) excited atoms, Ar^+ and Ar_2^+ ions. The relevant chemical reactions are listed in Table A.1 in the Appendix, and are adopted from Ref [32,35]. The chemistry in this argon model has been evaluated before, in a comparison between model [37] and experimental results, for the electron number density. In Ref [38], the electron number density in an Ar gliding arc was estimated as 9.7×10^{19} m^{-3}, for a current density of 10^5 A/m^2. In Ref [39], the electron number density in an Ar gliding arc (mixed with <2% H_2), derived from the Stark broadening of the H-beta line, was reported to be 2×10^{20} m^{-3}. Our simulations thus agree well with these experimental results. Therefore, we believe that the chemistry in our model is sufficient for the purpose of this work. We believe that the Ar (4s) radiative states can be neglected, because their radiation would be trapped in these atmospheric pressure conditions, and they are included in the lumped Ar (4s) species.

For the 2D-CS model in CO_2, 40 species are included (see Table 1), which react in more than 900 reactions (see Table A.2 in the Appendix). We pay special attention to the vibrationally excited levels of CO_2, as they are important for energy-efficient CO_2 conversion. Hence, we consider all the levels of the asymmetric stretch mode, up to the dissociation limit, i.e., 21 levels. However, to save calculation time, we lump them into three effective levels. In addition, we also consider four effective levels, representing the symmetric stretch and bending modes of CO_2, and three vibrational levels for O_2. The influence of excited CO was not included. In Ref [40], a comparison was made between models using a full chemistry set (including 63 CO vibrational levels [41]) and a reduced chemistry set (without excited CO levels, as used in our paper). The results showed that the influence of the excited states removed from the full chemistry set on the distribution of species number densities was negligible. The relative difference of CO_2 conversion predicted by the full and the reduced chemistry sets at 1 bar was only 1.2 %. The present experimental conditions are close to what was considered in [40]. Given the relatively low CO density in our results, we believe the assumption of the negligible influence of the excited CO levels is valid.

More details about the chemistry set and treatment of the vibrational levels are available in Ref [20,40]. For example, the vibrational excitation lowers the energy barrier for chemical reactions between two neutral molecules. We use the following formula for the reaction rate coefficient to consider this effect [42,43]:

$$k = A_0 \exp(-\frac{E_a - \alpha E_v}{T}) \tag{9}$$

where E_a is the activation energy of the reaction, E_v is the energy of the vibrational level and α is the parameter determining the efficiency of lowering the reaction barrier by vibrational excitation [44].

Table 1 Species included in the 2D-CS model in CO_2

Neutral ground state species	CO_2, CO, C, O, O_2
Neutral species in excited states	$CO_2[v_a]$, $CO_2[v_b]$, $CO_2[v_c]$, $CO_2[v_d]$, $CO_2[v_1\text{-}v_{21}]$, $CO_2[e]$, $O_2[v_1\text{-}v_3]$,
Charged species	CO_2^+, O_2^+, CO_3^-, O_2^-, O^-, e

4. Results and discussion

4.1 Experimental characterization of the MGA in argon and CO_2

Figure 3 shows the images of the arc motion taken by the high-speed camera, both for argon and CO_2, for three different gas flow rates and at three different times. Under the effect of the Lorentz force and swirling gas flow, the MGA rotates counterclockwise around the anode. The high-speed camera is manually triggered to record images only when the arc plasma is rotating steadily. The process of arc ignition and stabilization is not included. Therefore, '0 ms' in Figure 3 is the initial recording moment of the high-speed camera, not the moment of arc ignition. The minimum feed gas flow rate needed for the steady rotation is 0.7 L/min for Ar and 0.5 L/min for CO_2. In general, the diameter of the MGA in Ar is greater than 1 mm, while it is only about 0.5 mm in CO_2. The Ar MGA at 2 L/min shows the largest plasma diameter (1.84mm). By superimposing the MGA images at successive times, the motion path of the anode spots can be drawn (cf. dashed inner circle in Figure 3). Because the anode is cone-shaped, the smaller the diameter of the inner circle, the closer the anode spot is to the tip of the anode. By increasing the gas flow rate to 6 L/min, the diameter of the inner circle increases, which means that the anode spots of the MGA in Ar and CO_2 move in the opposite direction of the z-axis in Figure 1.

For the MGA in CO_2 at high gas flow rate (shown in Figure 3 for 6 L/min, but it already occurs above 4 L/min), after the arc elongates to a critical length (around 40 mm), a new short arc (around 9 mm) is suddenly formed behind the old arc channel. Subsequently, the emission intensity of the old arc channel quickly decays with time. The cathode spots of the new and old arc coincide, and the anode spot of the new arc lags behind the old one, as was also described in [15]. Such formation of a new discharge channel is similar to the back-breakdown phenomenon in the classical GA [35,45].

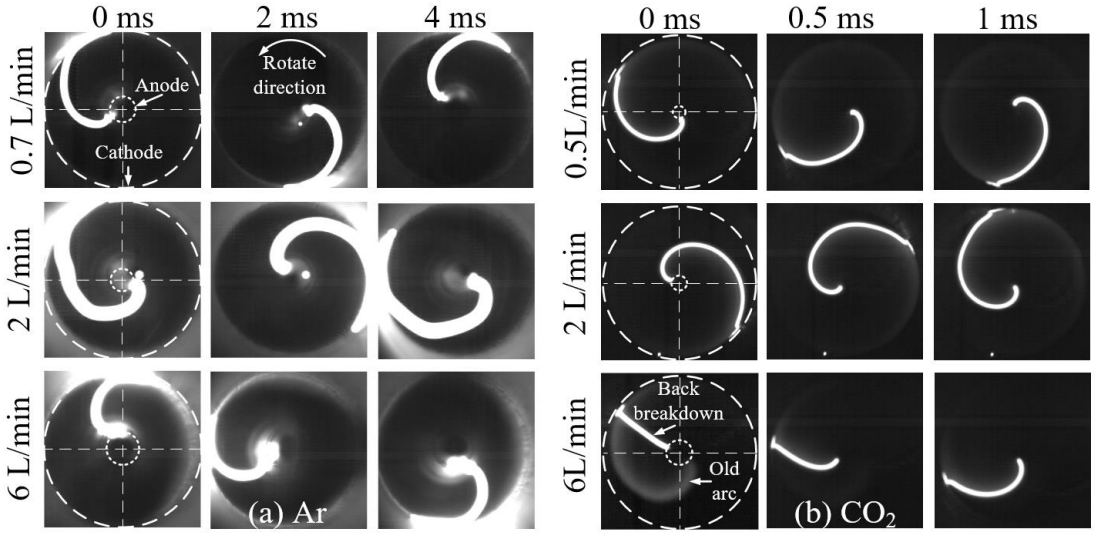

Figure 3: Dynamic behavior of the MGA in (a) Ar and (b) CO_2, obtained from end-on high-speed camera measurements.

For the MGA in Ar, the average arc voltage is 300 V for 0.7 L/min and 244 V for 6 L/min. The arc voltage of the CO_2 MGA is much higher, around 1400 V. The arc current is around 240 mA in Ar and 210 mA in CO_2. Figure 4 shows the voltage waveform of the MGA in CO_2 at two different gas flow rates, i.e., 0.5 L/min and 6 L/min. Both voltage waveforms exhibit periodicity. The voltage waveform at 0.5 L/min shows a smooth increase and decrease and the period of the sinusoidal shape waveform is around 2.5 ms. At 6 L/min there is a sharp drop in voltage (at a rate of 15 MV/s), which indicates the sudden shortening in arc length, corresponding to the back-breakdown phenomenon, as shown in Figure 3(b).

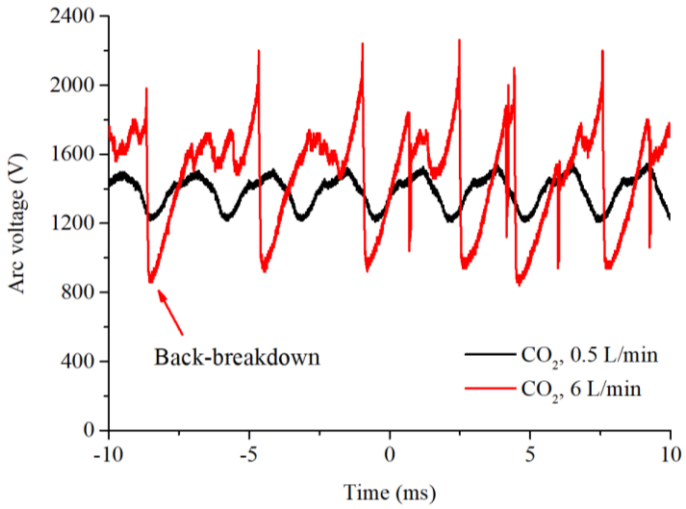

Figure 4: Arc voltage waveform of the MGA in CO_2 at two different gas flow rates

Table 2 Rotation frequency and arc length of the MGAs in Ar and CO_2 at different feed gas flow rates

Parameters \ Gas & flow rate (L/min)	Ar			CO_2		
	0.7	2	6	0.5	2	6
Rotation frequency (rps)	205	288	139	375	354	282
Arc length (mm)	12.4	19.1	13.9	22.4	25.3	26.5

Table 2 lists the rotation frequency and arc length of the MGAs in Ar and CO_2 at different gas flow rates. These parameters are derived by analyzing the high-speed camera images. Just like the arc voltage waveforms, the arc length varies with time, even at a constant gas flow rate. Therefore, the listed parameters are the average over three full rotating periods. Due to the limitation of the reactor structure, it is difficult to obtain information of the arc plasma in the axial direction of the reactor. The measured arc length is based on the line-of-sight images, which is the projection of the MGA in the z-axis of Figure 1 [46]. As the gas flow rate increases, the rotation frequency of the CO_2 MGA decreases and the arc length increases, but the MGAs in Ar do not present a similar trend. In our previous work [24], the rotation frequency and arc length were measured and compared for a MGA in N_2 and air. The change in gas flow rate affects the degree of turbulence inside the reactor, the attachment position of the arc spot and the possible back-breakdown phenomenon. A quantitative explanation about the change in rotation frequency and arc length at different gas flow rates and feed gases is difficult and beyond the scope of this paper. However, the dynamics of the MGA at low gas flow rate, where the effect of the Lorentz force dominates, can be used to validate the corresponding modeling results. For example, the rotation frequency of the MGA in Ar at 0.7 L/min is 205 rps, which is almost half of the value in CO_2 at 0.5 L/min (375 rps).

The measured electron temperatures as a function of Ar gas flow rate are shown in Figure 5. Increasing the gas flow rate from 2 L/min to 16 L/min causes a drop in electron temperature from 2.01 eV to 1.07 eV. This can be explained because the arc voltage decreases upon higher gas flow rate, as written above. Thus, as the total energy input decreases, the electrons gain less energy, so the electron temperature decreases with increasing gas flow rate. The same trend was reported in Ref [47].

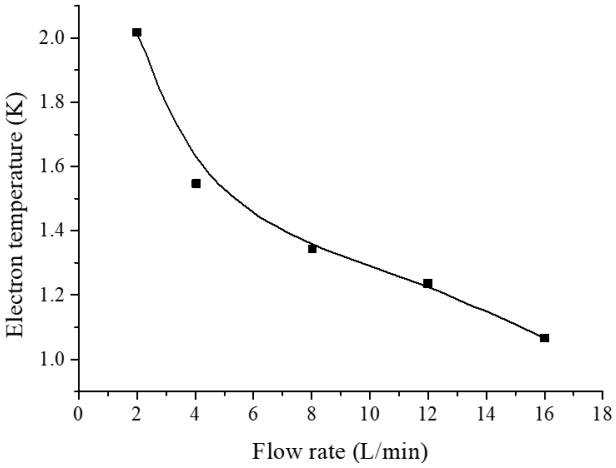

Figure 5: Measured electron temperature of the MGA in Ar as a function of gas flow rate, obtained by OES

4.2 3D-MGA model in argon

The calculated gas temperature distribution of the MGA in argon is shown in Figure 6(a,b) at two different times. At t = 0.1 ms, the arc is just initiated at the x-axis; see Figure 6(a). The arc body shows a thin cylindrical profile due to the artificial heating term. Under the effect of the external magnetic field, a Lorentz force in the y-direction is generated, and it drives the arc bending and rotating counterclockwise, as illustrated in Figure 6(b) for t = 1.2 ms. Figure 6(c) is a cut plane of Figure 6(b) at x = 3 mm (cf. dashed rectangle in Figure 6(b)). In addition, the white arrows in Figure 6(c) represent the velocity distribution. It can be seen that only the plasma with high gas temperature exhibits a high moving speed (maximum velocity 7 m/s on the symmetry plane), while the remaining 'cold' region on the plasma plane has almost no gas flow. Indeed, the Lorentz force is the only driving force in the 3D-MGA model. The high gas temperature region has a higher electric conductivity and current density, so it experiences a greater Lorentz force. In GDGAs, the feed gas flow moves faster than the arc column, which is opposite to the situation of the MGA.

For GDGAs, the velocity difference between the arc column and the feed gas flow was investigated both experimentally [48] and theoretically [19,49]. It is believed that a larger velocity difference increases the fraction of gas treated by the plasma, and thus it can enhance the gas conversion. In addition, the larger the velocity of the feed gas, the greater will be the velocity difference. Therefore, several modifications were made to GA reactors (mainly classical GA designs) to increase the feed gas velocity, like shortening the distance between the nozzle outlet and the electrodes and reducing the inner diameter of the nozzle [50,51].

In contrast, the velocity difference in MGAs was less investigated. The relative velocities were calculated to be 4.2-10.4 m/s in Ref [16], and 2-8 m/s in Ref [22], when the Lorentz force and aerodynamic drag force from the surrounding gas were equal. The calculated velocities of our 3D-MGA model (maximum velocity 7 m/s; cf. above) are within the range of the measured values. In Ref [16,22], a Lorentz force opposite to the feed gas flow was generated by reversing the polarity of the ring magnet. By tuning the feed gas flow rate, the arc may twist without rotating. This means that the effect of the Lorentz force acting on the GA is equivalent to a certain feed gas flow rate. It is also worth noting that the influence of the Lorentz force on the arc is almost constant at a fixed arc current and external magnetic field. Therefore, the contribution from the Lorentz force on the relative velocity is more dominant at lower feed gas flow rates, for example, at zero gas flow rate, as in our 3D-MGA model. The large relative velocity between the GA and the surrounding feed gas in a MGA could be advantageous to increase the fraction of gas treated by the plasma, and thus the reactor's performance for gas conversion, especially when working at low feed gas flow rates.

Another significant difference between the MGA and GDGA is that the temperature distribution within a cross-section of the MGA shows a crescent shape (see Figure 6(c)), instead of an elliptical shape in the GDGA. The cross section of the plasma without magnetic field and gas flow is simply a circle [36]. To illustrate the latter, we plot in Figure 7 the typical temperature distribution in a GDGA, calculated for a classical GA in Ar at 28 mA [49]. The different shape in the temperature distribution between Figure 6(c) and Figure 7 is clearly visible.

While the MGA rotates around the axis of the plasma plane, two vortices are formed on both sides of the symmetry plane, which will introduce the surrounding cold gas into the back end of the arc. This results in two 'tails' behind the arc core, which also exhibit a high gas temperature (around 1500 K, vs. almost 2300 K in the center) and electron number density (around 10^{19} m^{-3} vs. above $2.2x10^{20}$ m^{-3} in the center; cf. Figure 6(c)). These may lead to a larger volume of interaction between the feed gas and plasma.

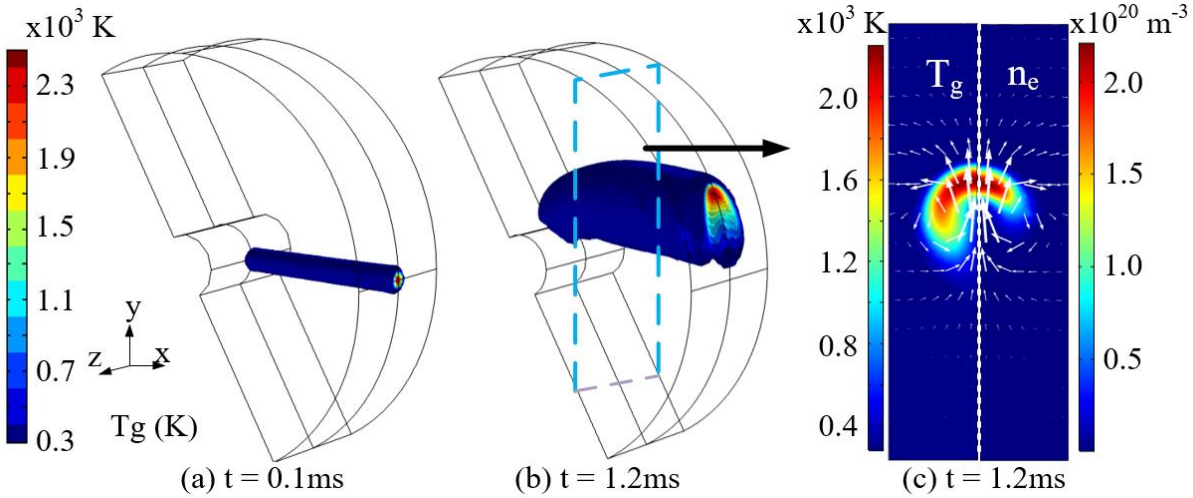

Figure 6: Gas temperature distribution at (a) t = 0.1 ms and (b) t = 1.2 ms in the 3D geometry, as well as gas temperature and electron number density in the cut plane at x = 3 mm (c) (cf. dashed rectangle in (b)), at t = 1.2 ms, 200 mA and 0.2 T. In (c) the left part of the figure shows the gas temperature, while the right part shows the electron number density. Moreover, also the gas velocity vectors are depicted by white arrows in (c).

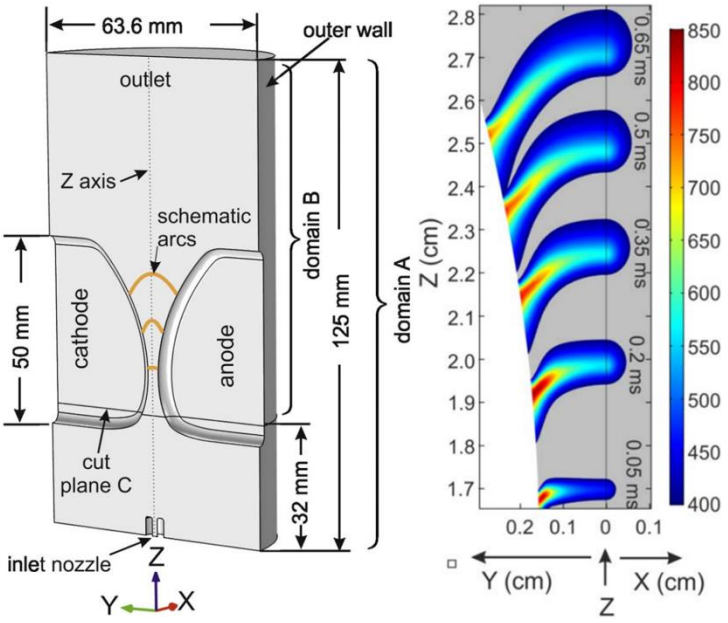

Figure 7: Geometry of a classical GDGA reactor (left) and calculated gas temperature distribution (right) in this reactor, calculated with a 3D model in Ar, at a discharge current of 28 mA and applied gas flow rate of 10 L/min. Adopted from [30] with permission of IOP.

Figure 8 shows the calculated electron number density, electron temperature, gas temperature and electric field in the symmetry plane (z = 0 mm) at t = 1.2 ms. The maximum electron density (Figure 8 (a)) is about 6.1×10^{20} m^{-3}, which is a typical value for a GA in argon [32], as also deduced from spectroscopic measurements [39]. The maximum electron temperature (Figure 8 (b)) is approximately 2.5 eV, which is almost ten times higher than the gas temperature (i.e., around 2500 K; Figure 8(c) and also Figure 6). It indicates that the Ar MGA is in strong non-equilibrium. Although our calculated electron temperature is higher than the measured values presented in Figure

5, considering that this temperature increases with decreasing feed gas flow rate, our calculated electron temperature (at 0 L/min) is within a reasonable range.

Note that the fluid equations in the drift-diffusion approximation assume a Maxwellian distribution. Depending on the operating conditions, a non-Maxwellian distribution can lead to different transport properties of the electrons and the ions. Sometimes these properties can differ by a factor of two or more. This can lead to differences in the plasma potential and the ambipolar electric field, which will affect the electron temperature. However, our model does not compute the EEDF self-consistently, and we do not have prior knowledge of a non-Maxwellian distribution in gliding arc plasmas from experiments. In previous papers [32,35], the electron temperature was also calculated to be around 2.5 eV using similar fluid equations (without magnetic field). Besides, the simplified chemistry may be the reason for the higher electron temperature compared to experiments: because of the underestimated ionization rate, a higher electron temperature is produced in order to sustain the discharge at a certain density. Another reason for the difference may be that the 3D-MGA model simulates the MGA without feed gas flow.

As shown in Figure 8, the arc is significantly bent, especially near the inner electrode. The bending is due to the no-slip boundary condition used in the model near the electrodes. Therefore, the arc near the electrodes is forced to move slower than the arc column. The shape of the arc agrees well with the images recorded by the high-speed camera, as illustrated in Figure 3(a). At t = 1.2ms, the arc length of the 3D-MGA model is around 11 mm, which is similar to the experimental arc length (12.4 mm) of the Ar MGA at 0.7 L/min, as listed in Table 2 above. In addition, Figure 6 and Figure 8 shows that the anode spot takes 1.2 ms to turn counterclockwise by 1/4 of the anode circumference. Therefore, the rotation frequency of the simulated anode spot is around 208 rps, which is similar to the experimental rotation frequency in the Ar MGA at 0.7 L/min (i.e., 205 rps; see also Table 2).

The electric field distribution is shown in Figure 8(d). The bending of the MGA leads to an inhomogeneous distribution of the electric field. Indeed, the electric field is more concentrated behind the arc moving direction (region 1 in Figure 8(d)) and close to the outer electrode (region 2, 4). The inner anode has a smaller diameter and a large curvature, so the electric field in region 3 is the strongest. After the arc moving, region 1 still has a relatively high electron number density (around 2×10^{19} m^{-3}). Therefore, the electron temperature in this regions is higher than in the surrounding feed gas. Especially, if the degree of arc bending can be further enhanced (by increasing the external magnetic field or by applying higher feed gas flow rates in the experiments), the electric field might be high enough to cause breakdown of the hot gas behind the arc moving direction. This would lead to a back-breakdown, followed by a significant drop in the arc voltage, as discussed in Sec 4.1 above. Hence, the MGA may operate in the so-called ‘restrike’ mode [24,52,53]. The cathode spot jumping would also affect the arc mode transition in the GA. However, a more detailed model would be needed for this, including a description of the plasma sheath [28], which is beyond the scope of this work.

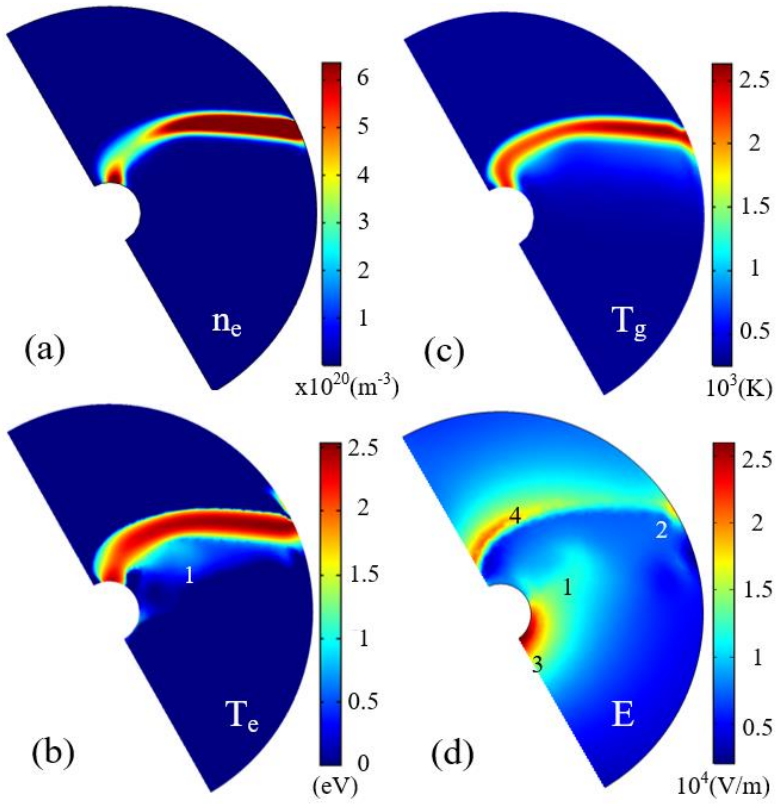

Figure 8 Electron number density (a), electron temperature (b), gas temperature (c) and electric field (d) in the symmetry plane of the MGA reactor (z = 0 mm, t = 1.2 ms) at 200 mA and 0.2 T.

To summarize, the MGA presents a higher moving speed than the feed gas flow, while the GDGA typically lags behind the gas flow. The cross section of the MGA exhibits a crescent shape, instead of an elliptical shape in the GDGA. In general, the results from the 3D-MGA model show that the MGA is indeed different from a traditional GDGA.

4.3 2D-CS model in argon: Effect of arc current and external magnetic field

In this section, we use the 2D-CS model to study the effect of arc current and external magnetic field on the arc characteristics, because this model is far less time-consuming than the 3D-MGA model. Indeed, it takes 20 hours to simulate the arc behavior over 2 ms with the 2D-CS mode, while the same simulation takes more than two weeks with the 3D-MGA model. In addition, the calculation results obtained with the 2D and 3D model are very similar, as will be illustrated below.

The arc is initiated at y = 1 mm (cf. Figure 2(b)). Under the effect of the external magnetic field, the arc moves downward. The gas temperature distribution at 0.5 ms and 1.2 ms after the arc ignition are shown in the upper right of Figure 9. The cross-section of the arc expands and shows a crescent shape, similar to the 3D-MGA model in Figure 6(c). Figure 9 also illustrates the evolution of gas temperature and electron density along the symmetry line (y-axis), for an arc current of 100 mA and external magnetic field of 0.2 T. The peak gas temperature is around 1600-1800 K and slowly decreases with time. The electron number density shows the same decreasing trend as the gas temperature, but a bit more pronounced, from 2.45x10^{20} m^{-3} at 0.3 ms to 0.84x10^{20} m^{-3} at 1.5 ms. The drop in T_g and n_e is due to the expansion of the arc cross-section as a function of time.

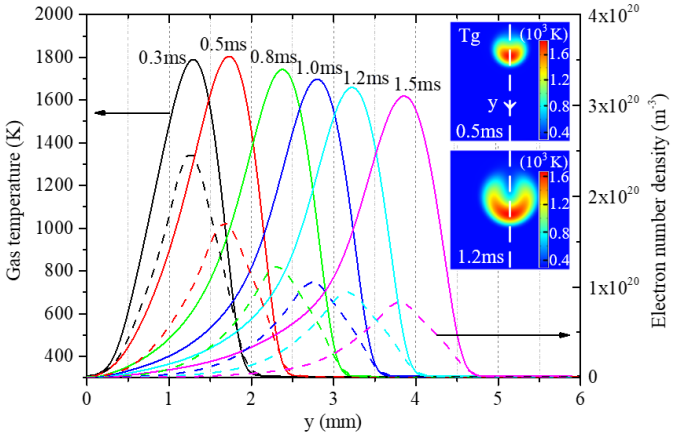

Figure 9 Evolution of gas temperature and electron number density of the MGA, as obtained from the 2D-CS model, for an arc current of 100 mA and external magnetic field (B_E) of 0.2 T. The inserts at the right illustrate the gas temperature distribution, at 0.5 and 1.2 ms after arc ignition.

Figure 10 shows the distribution of velocity, gas temperature, electron temperature and electron number density at an arc current of 200 mA, for two different external magnetic fields, i.e., B_E = 0.1 T and 0.2 T, at t = 1.4 ms. For the same arc current, increasing the external magnetic field leads to a higher Lorentz force and a higher arc moving velocity. The arc motion at B_E = 0.2 T is indeed significantly faster than at B_E = 0.1 T, i.e., the arc core is more compressed and the two 'tails' are more obvious. We can compare the results of the 3D-MGA and 2D-CS model (at similar conditions: DC 200 mA, 0.2 T, Figure 8 and Figure 10), to check the validity of the 2D-CS model. The maximum electron temperature of the 2D-CS model is in the order of 2.45 eV, similar to T_e in the 3D-MGA model (2.5 eV). The maximum gas temperature and electron number density of the 2D-CS model are around 2000 K and $1.3\text{x}10^{20}$ m^{-3}, which is smaller than the maximum T_g (around 2500 K) and n_e ($6\text{x}10^{20}$ m^{-3}) in Figure 8. However, at the arc column, where the effect of the electrodes (small velocity due to no-slip boundary condition) is less significant, T_g and n_e are comparable to the values of the 2D-CS model, for example 2200 K and $2.2\text{x}10^{20}$ m^{-3} in Figure 6(c).

Note that we cannot compare the calculated electric field from the 2D and 3D model. Indeed, the 2D model assumes that the gliding arc exists between two parallel electrodes and the arc current flows along the x-axis without bending. It simulates a slice (y-z plane, perpendicular to the current) between the two electrodes. There is no need to solve the electric potential equation. The current density is defined by $J \propto \sigma$ and a fixed total arc current $I_{tot} = \int Jds$ on the slice. Under such assumptions, the electric field should be homogeneous (about 10^4 V/m here) in the 2D model. On the other hand, in the 3D model, an inhomogeneous distribution of the electric field is obtained, due to the different shapes of the electrodes and the arc bending, which cannot be described in the 2D cross section model. Therefore, the 2D model is more suitable for modeling the part of the GA that is far from the electrodes.

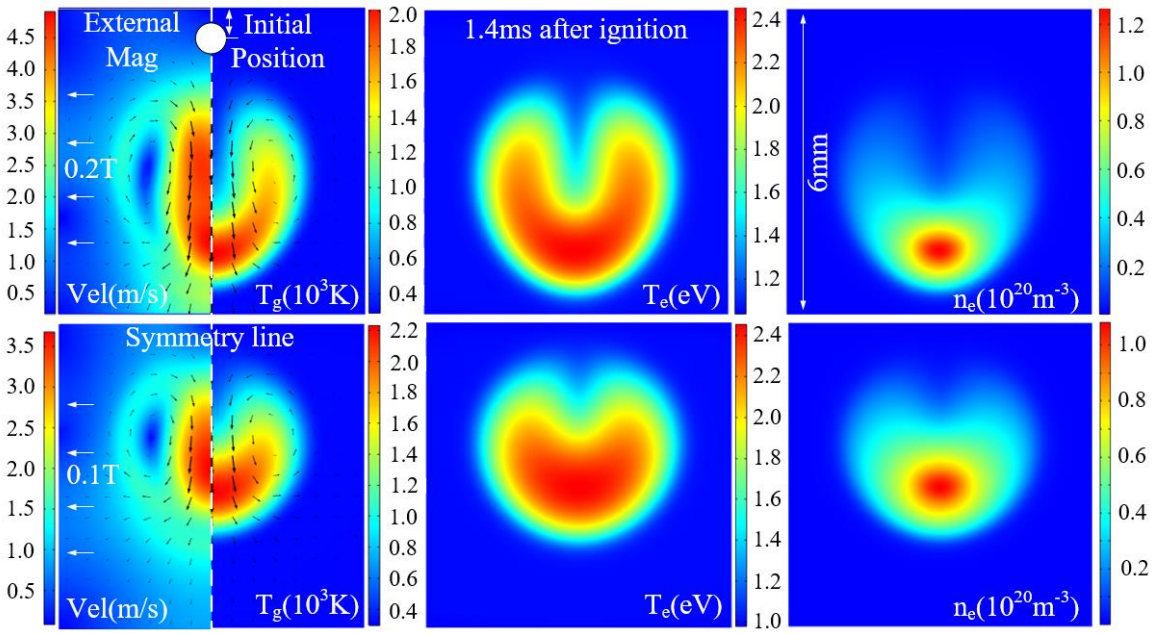

Figure 10 2D plots of velocity and gas temperature (left), electron temperature (middle) and electron density (right), for two different external magnetic fields (top: 0.2 T, bottom: 0.1 T), at 1.4 ms after arc ignition, for an arc current of 200 mA. The black arrows in the left figures represent the velocity vector.

The effect of the magnetic field on the MGA behavior is presented in more detail in Figure 11. The maximum magnetic field investigated is 0.4 T. Indeed, from the perspective of energy saving and portability, the external magnetic field in experiments of MGAs is generated by permanent magnets rather than by electromagnets. Normally, rare-earth permanent magnets can produce a magnetic field of 1 T on their surface, but from engineering point of view, 0.4 T should be achievable, while larger magnetic fields might be difficult. The peak T_g decreases with increasing B_E, from 2446 K at 0.05 T to 1871 K at 0.4 T. At the same time, the width (full width at half maximum, FWHM) of the T_g profile along the y-axis also decreases, from 1.9 mm at 0.05 T to 1.0 mm at 0.4 T. The change in n_e upon increasing magnetic field is, however, opposite to the change in T_g. The peak n_e is almost constant when B_E varies between 0.05 T and 0.2 T, but it suddenly increases by 30% from 0.2 to 0.4 T.

The drop in gas temperature upon increasing B_E is due to the stronger energy transport between the plasma and the cold surrounding gas, more specifically, via convection. The velocity of the arc movement increases upon rising magnetic field, as is clear from Figure 11. The velocity of the MGA is the relative velocity between the plasma and the cold surrounding gas. Hence, the arc cooling is greatly enhanced by stronger convection under higher B_E. This might be beneficial for gas conversion, as it enhances the non-equilibrium character of the GA, exploiting better the vibrational dissociation pathway for CO_2 conversion [1,13,21,54], although it should be realized that the present results are obtained for argon. In GDGAs, the gas temperature of the arc can be reduced by increasing the gas flow rate and changing the flow pattern inside the reactor [30,36]. Increasing the amount of cold feed gas will definitely enhance heat transfer, and reduce the gas temperature. In addition, the purpose of changing the flow pattern is to create a higher degree of turbulence, because the turbulent thermal conductivity is also effective in reducing the gas temperature by enhancing turbulent heat transfer [30]. However, both the plasma-feed gas reaction time (i.e., residence time of the feed gas in the plasma) and the specific energy input will drop upon increasing gas flow rate, which has a negative effect on the gas conversion [50,55]. In contrast, an external magnetic field can reduce the gas temperature without introducing this undesired 'side effect' by increasing the flow rate, stressing the advantage of a MGA.

The increase in electron number density upon increasing B_E in a MGA (see Figure 11(b)) is mainly due to a more compressed arc shape (cf. Figure 10). This higher electron density can also be beneficial for gas conversion. One of the most important CO_2 conversion pathways in a GA is electron impact dissociation from the CO_2 vibrational levels ($CO_2(v) + e \rightarrow CO + O + e$) [20]. Increasing the electron number density will promote the vibrational excitation [19]. It has been reported that plasma reactors present a higher CO_2 conversion rate by mixing with argon [15,56–58], which is easier to ionize and helps to increase the electron number density. The 'side effect' of dilution by Ar and other gases lies in the drop of energy efficiency due to extra energy consumption in the diluting

gas and additional cost to separate the diluting gas after plasma processing. Such 'side effect' from gas dilution is avoided and the increase in electron number density can be achieved at the same time using an external magnetic field, which is again an advantage of a MGA.

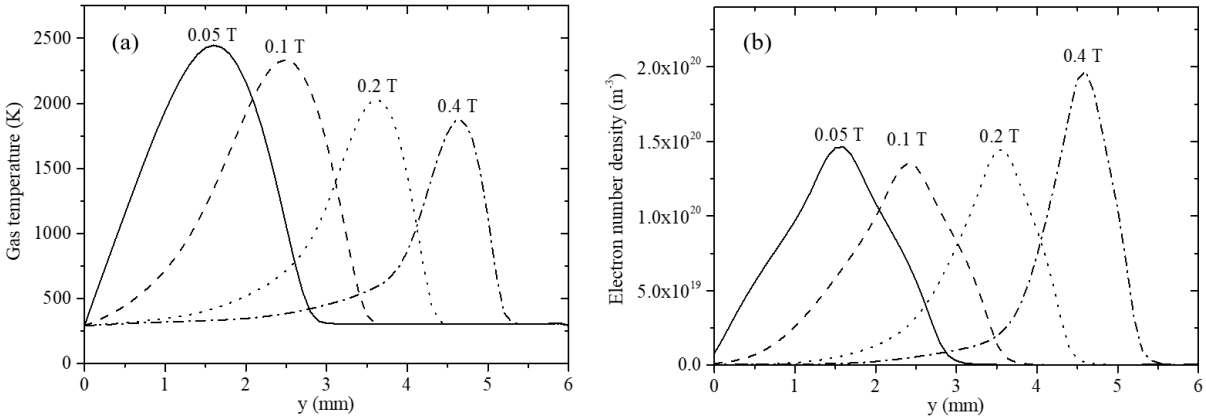

Figure 11: Distribution of (a) gas temperature and (b) electron number density along the y-axis for the MGA for different external magnetic fields (0.05 T - 0.4 T) at t = 1 ms. The arc current is 200 mA.

Figure 12 shows the peak T_g, T_e, n_e and maximum velocity along the y-axis as a function of arc current, for different magnetic fields. The peak gas temperature and electron number density rise significantly with increasing arc current, e.g., from 1400 K, 0.74×10^{20} m^{-3} at 50 mA to 2470 K, 1.95×10^{20} m^{-3} at 400 mA (for B_E = 0.2 T). The maximum velocity shows a similar trend as n_e upon rising arc current. A higher arc current and stronger magnetic field both yield a higher arc moving velocity. However, since the additional cooling due to the higher velocity is less pronounced than the increase in injected energy upon higher arc current, the gas temperature still rises with rising arc current. On the other hand, a higher B_E results in a lower peak gas temperature, as is clear from Figure 12(a), and was also presented in Figure 11(a). The effect of B_E on reducing T_g is more effective at higher arc current. Nevertheless, the drop in T_g e.g., by doubling B_E cannot compensate for the rise in T_g by doubling the arc current (e.g., cf. T_g at 100 mA and 0.10 T vs. at 200 mA and 0.2 T). On the other hand, the maximum electron temperature is virtually constant (around 2.4 - 2.5 eV), for different values of arc current and magnetic field. A similar trend upon rising arc current was also reported in Ref [14]. A higher arc current leads to more pronounced Joule heating on electrons. On the other hand, the electron number density also increases upon increasing arc current, which is logical. Therefore, the higher power resulting from the higher current will have to be distributed over more electrons, so that the average electron energy stays constant.

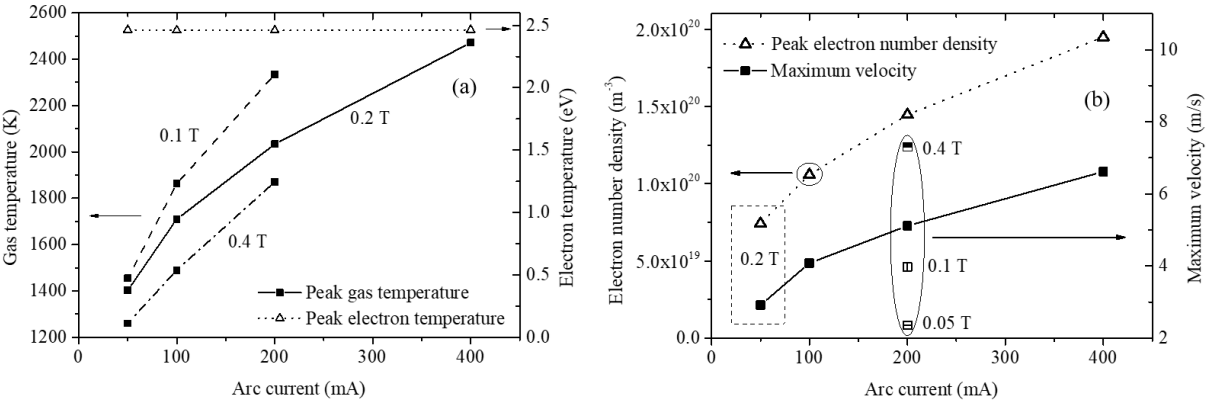

Figure 12: The peak (a) gas temperature, electron temperature, (b) electron number density and maximum velocity along the y-axis for the MGA, as a function of arc current (50 - 400 mA), at different values of magnetic field (B_E = 0.05 - 0.4 T), at t = 1.0 ms.

4.4 2D-CS model in CO_2: Consequences for CO_2 conversion

GA reactors are very promising for CO_2 conversion, so it is more interesting to investigate the MGA behavior in CO_2. The large number of species and reactions that must be included in the CO_2 GA model require extensive computation resources. Furthermore, the necessity of the coupled solution of the flow equations and plasma equations in the MGA makes the computation even slower. Therefore, the MGA in CO_2 is only investigated using the 2D-CS model.

Figure 13 (a) shows the T_g and n_e distribution of the MGA in CO_2, 1.0 ms after ignition. Both T_g (left) and n_e (right) exhibit crescent shapes, just like for the Ar MGA in Figure 10. Figure 13 (b) presents the peak gas temperature, vibrational temperature (T_v) and n_e along the y-axis, at 0.5 and 1 ms after ignition. Both temperatures and the electron density slightly decrease as a function of time. The maximum T_g is about 3370 K, which is about 1000 K higher than in the Ar MGA at the same arc current and external magnetic field. Indeed, the presence of several different vibrational excitation levels in CO_2 leads to a higher plasma temperature due to vibrational-translational (VT) relaxation [30]. As is clear from Figure 13 (a), there is a large volume of hot gas behind the arc core, with T_g around 2000-3000 K. The peak electron temperature is around 1.6 eV for the CO_2 MGA, which is much lower than in argon (2.4 – 2.5 eV). Indeed, the electrons can lose more energy in the CO_2 plasma, because of the many extra electron energy loss channels, such as electron impact dissociation and vibrational excitation. Therefore, the degree of non-equilibrium in the CO_2 MGA (1.6 eV for T_e vs. 3370 K for T_g) is smaller than in the Ar MGA (2.5 eV vs. 2330K), but there is still a significant difference between T_e and T_g. The peak electron number density of the CO_2 MGA is around 4×10^{19} m^{-3}, nearly four times lower than in Ar. This can be explained by the loss of electrons due to electron attachment with CO_2, which is not occurring with argon. In addition, the electrons lose energy by vibrational excitation and dissociation of CO_2, so the same amount of power leads to a lower ionization degree, and thus a lower electron number density, in the CO_2 plasma.

In addition, the electron density in the CO_2 MGA is more concentrated than in the argon MGA (cf. Figure 10). The width (FWHM) of the n_e profile along the y-axis is around 0.5 mm in CO_2, while it is 1.6 mm in argon. It is more difficult to ionize CO_2 than Ar, so CO_2 requires a more concentrated current density to produce free electrons. As a result, the plasma power density is higher, which also leads to a higher temperature. The latter causes a significant thermal contraction in the arc. The contraction is enhanced further by the chemical reactions. Therefore, the CO_2 plasma is thinner, as predicted by our model, and obtained from the experiments (see Figure 3). The high-speed camera measurements also indicated a thinner arc column in CO_2 (see Figure 3). Large gradients in n_e distribution can thus be observed, and therefore, a finer mesh was needed for the simulation of the MGA in CO_2, further increasing the computation time. The current density, which has a similar distribution as the electron number density, is more concentrated in the CO_2 MGA than in Ar. Therefore, the CO_2 MGA moves with a larger velocity, due to the stronger Lorentz force. At the same current and external magnetic field (e.g. 200 mA and 0.1 T), the peak of n_e moves 2.9 mm within 1 ms in CO_2 while only 1.4 mm in Ar (cf. Figure 11). This result is also supported by the experiments. Indeed, Table 2 showed that the arc rotation frequency of the MGA in CO_2 (375 Hz) is almost twice that of the MGA in Ar (205 Hz).

Validation of the results of the CO_2 gliding arc model is more difficult, due to lack of experimental data (i.e., lack of suitable emission lines in CO_2 plasma). The available experimental data are from CO_2 gas mixtures. In Ref [59], the gas temperature (2700 K) and vibrational temperature (6000 K) were measured in 95% CO_2-5% N_2 mixture at relatively large gas flow rate (10 L/min). For the MGA, the measured vibrational temperature was 3200-3700 K in air [14]. Hence, our calculation result is within the experimental range. However, these experiments were not performed for our MGA, and it is difficult to exactly compare different gliding arc configurations under different discharge conditions.

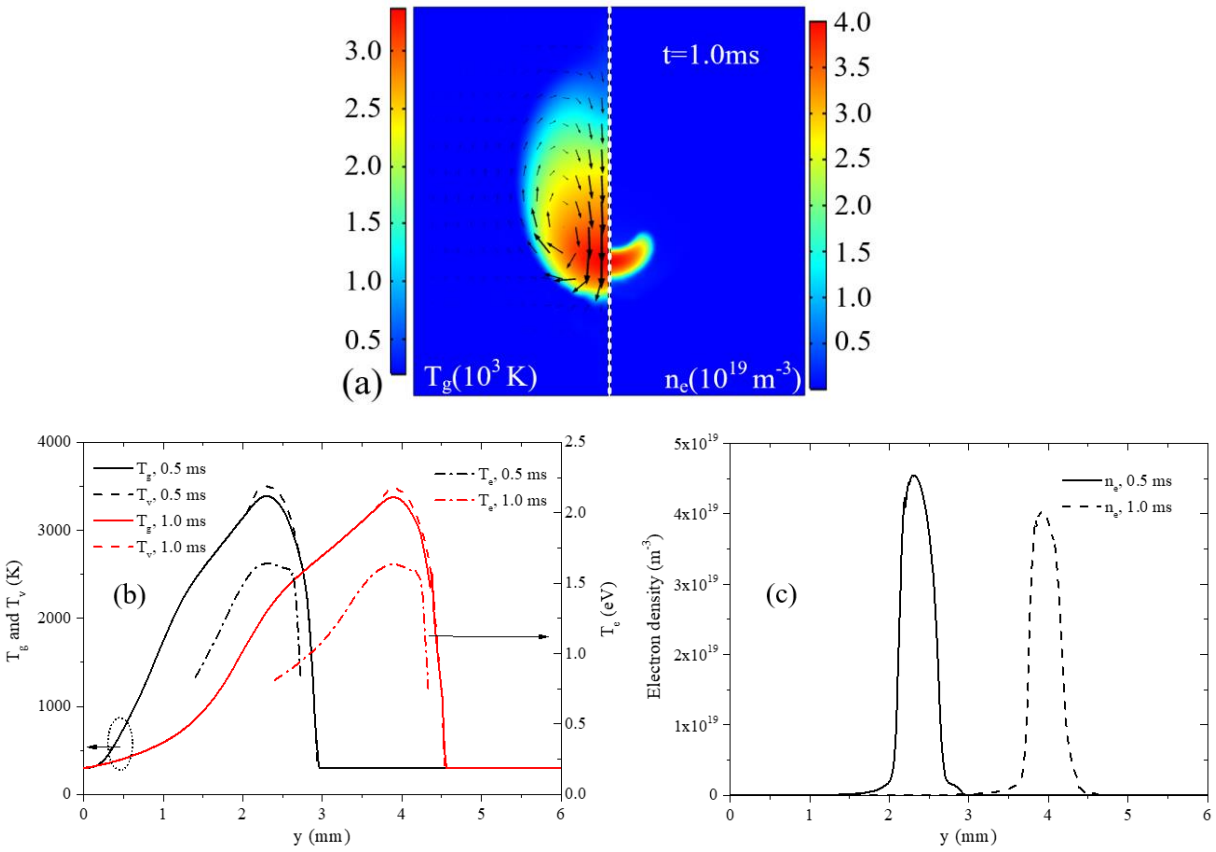

Figure 13: 2D distribution of (a) gas temperature and electron density in the plasma. The black arrows are the velocity vectors. (b) Gas and vibrational temperature, electron temperature and (c) electron number density along the y-axis for the CO_2 MGA, 0.5 and 1 ms after arc ignition. The arc current is 200 mA, and B_E = 0.1 T.

The vibrational temperature is almost the same as the gas temperature. It is only about 100 K higher in the arc centre. A similar result was also obtained in Ref [30] for a GDGA (GAP). The fact that T_g and T_v are nearly the same indicates that the vibrational energy distribution function of CO_2 in the MGA is very close to an equilibrium Boltzmann distribution, defined by the gas temperature. This will limit the performance of the MGA for energy-efficient CO_2 conversion, because the latter is only fully exploited if the high vibrational levels of CO_2 are overpopulated, and the energy loss by VT relaxation is limited. Our simulations suggest that such overpopulation cannot be easily achieved upon applying an external magnetic field. However, by tuning the external magnetic field and arc current, a lower gas temperature can be achieved, as discussed in Sec 4.3. For plasma-based CO_2 conversion, reducing the gas temperature of the GA might be beneficial, as it enhances the vibrational-translation non-equilibrium, giving rise to more energy-efficient conversion, and in addition, the conversion will also be higher, due to less significant recombination of CO and O at lower temperature. Previous simulation results [21] also showed the overpopulation of the vibrational levels of CO_2 is only significant at quite low gas temperature (< 1200 K). The conversion and energy efficiency might theoretically reach 18% and 96%, respectively, which is much higher than all the GA experimental results obtained so far and very attractive for further industrial applications. Such a low temperature cannot be achieved only by applying a sufficient magnetic field that is feasible from engineering point of view. A more effective way to reduce the gas temperature is to reduce the arc current. However, the Lorentz force decreases with decreasing current, which greatly reduces the effect of the applied magnetic field. On the other hand, the magnetic field enhances the plasma volume, as shown in Figure 6 and Figure 13 above, so that more gas can be treated by the plasma, which will be beneficial for enhancing the CO_2 conversion. The possible enhancement in CO_2 conversion was validated by a recently published paper [17]. The effect of external magnetic field on the CO_2 conversion was investigated experimentally, and we found that an external magnetic field significantly improved the CO_2 conversion in the GA, from 8.2 % to 11.5 % (for a magnetic field of 0.5 T, and a gas flow rate of 1 L/min), and also the energy efficiency increased from 5.8 % to 8.0 %.

Figure 14 shows the mole fractions of the main species produced by CO_2 conversion, i.e., CO, O and O_2, as well as CO_2 itself, as a function of position along the y-axis, 0.8 ms after arc ignition. In the arc core, the mole fraction

of CO_2 is less than 10%, which indicates that most of the CO_2 molecules are split into CO, O and O_2. Behind the direction of plasma movement, there is still a considerable part of CO_2 converted. Although the electron number density quickly decreases to values lower than 10^{19} m^{-3}, the gas temperature is still very high after the arc core, still allowing thermal conversion of CO_2.

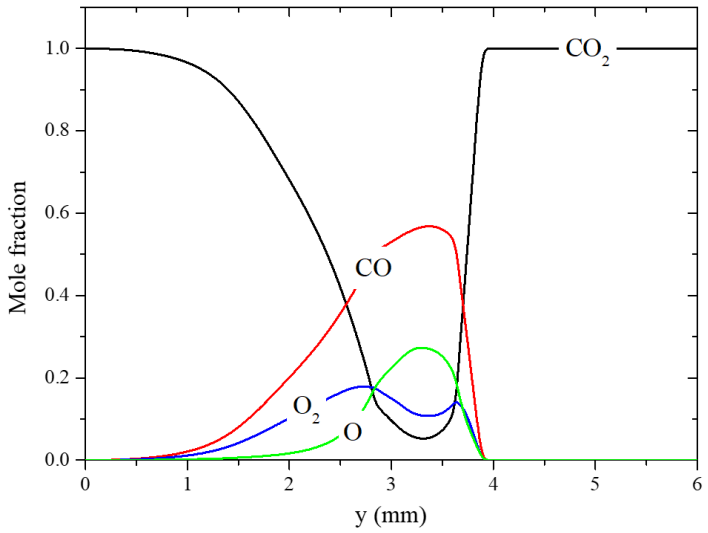

Figure 14: Calculated mole fractions of CO_2, CO, O and O_2 along the y-axis, for the CO_2 MGA. Arc current = 200 mA, B_E = 0.1 T, t = 0.8 ms.

To better understand the CO_2 conversion mechanisms, the reactions leading to CO_2 dissociation are listed in Table 3 and their reaction rates as a function of time are plotted in Figure 15. The reaction rates are the spatial integration over the 2D simulation plane. The reaction rate coefficients of these reactions can be found in Table A.2. They were adopted from [42].

The reactions of CO_2 vibrationally excited molecules with either O atoms or any neutral species (typically molecules, because of their highest density) (i.e., $CO_2(v) + O \rightarrow CO + O_2$ (L2), and $CO_2(v) + M \rightarrow CO + O + M$ (L3)) are the dominant CO_2 dissociation reactions at the conditions under study. Especially the dissociation of vibrationally excited CO_2 molecules upon collision with O atoms (L2v) is the most important reaction, with a contribution around 75 %. This indicates that the vibrationally excited levels of CO_2 play an important role in CO_2 conversion. The same process, but with CO_2 ground state molecules (L2g) contributes for only 8 %. The dissociation of vibrationally excited CO_2 with any neutral species (L3v) contributes for around 15%. Electron impact dissociation of CO_2 (L1) contributes for only 0.7% in total, but again occurs about ten times faster from the CO_2 vibrational levels than from the ground state. The other reactions listed in Table 3 (L4-L7) are virtually negligible. We only present the simulation results at 0.1 T. While there might be a reason to believe that the plasma chemistry will change as a function of the magnetic field, we think the same reactions will be dominant. Indeed, in previous work of a GDGA in CO_2 , i.e., without magnetic field [19], reactions L2 and L3 were also found as the dominant CO_2 conversion pathways. We believe the main reason for the enhanced CO_2 conversion is that the magnetic field influences the arc shape and rotation speed, which affects the fraction of gas treated by the arc and the power deposition, and this will affect the CO_2 conversion and gas temperature, respectively.

Our calculations predict that the dissociation of vibrationally excited CO_2 upon collision with O atoms (reaction L2v in Table 3) is the main CO_2 loss process and the vibrationally excited levels play a dominant role in CO_2 decomposition. Although the vibrational energy distribution of CO_2 is close to a Boltzmann distribution and the higher vibrational levels of CO_2 are not overpopulated, the number densities of the CO_2 low asymmetric and symmetric vibrational levels are still high. Besides, the reaction rate coefficients increase for higher vibrational levels, as discussed in Section 3.

Table 3 Overview of the CO_2 dissociation reactions

No.	Reactions
L1v	$e + CO_2(v) \rightarrow e + CO + O$
L1g	$e + CO_2(g) \rightarrow e + CO + O$
L2v	$CO_2(v) + O \rightarrow CO + O_2$

L2g	$CO_2(g) + O \rightarrow CO + O_2$
L3v	$CO_2(v) + M \rightarrow CO + O + M$
L3g	$CO_2(g) + M \rightarrow CO + O + M$
L4v	$O^- + CO_2(v) + M \rightarrow CO_3^- + M$
L4g	$O^- + CO_2(g) + M \rightarrow CO_3^- + M$
L5v	$e + CO_2(v) \rightarrow e + e + CO_2^+$
L5g	$e + CO_2(g) \rightarrow e + e + CO_2^+$
L6v	$e + CO_2(v) \rightarrow CO + O^-$
L6g	$e + CO_2(g) \rightarrow CO + O^-$
L7v	$CO_2(v) + C \rightarrow CO + CO$
L7g	$CO_2(g) + C \rightarrow CO + CO$

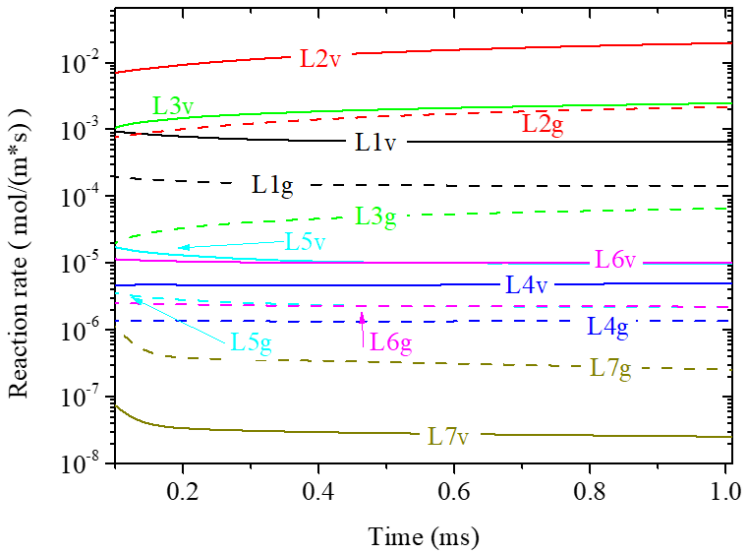

Figure 15 Time evolution of the reaction rates of the different CO_2 dissociation pathways, spatially integrated over the simulation plane. The notations of the reactions are given in Table 3.

5. Conclusion

We presented two fully coupled flow-plasma models, to describe the arc dynamics and plasma behavior in an MGA in argon and in CO_2. We developed a 3D argon plasma model to investigate the dynamic behaviour of the GA under the influence of an external magnetic field and to reveal the differences between an MGA and a GDGA. The Lorentz force leads to a considerable relative velocity between the MGA and the cold feed gas, which will be helpful to increase the fraction of gas treated by the GA. The arc shape and rotating motion, the gas temperature, electron number density and electron temperature predicted by the 3D model are in reasonable agreement with experimental results from our experiments and from literature.

To study the effect of the external magnetic field, in combination with the arc current, on the GA behavior, we also developed a 2D cross-section model, which is less computationally intensive, and allows to run the model for a wider range of conditions with reasonable computation resources. Our model predicts that the magnetic field can enhance cooling, so it can be an effective way to control the GA gas temperature and electron number density. The 2D cross-section model in CO_2 indicates that the MGA shows a strong non-equilibrium between electron temperature and gas temperature. On the other hand, the vibrational energy distribution function of CO_2 is close to a Boltzmann distribution at the gas temperature, and does not exhibit overpopulation of the high vibrational levels. Inside the arc, the splitting of CO_2 is nearly complete, and plenty of CO_2 is still converted at the high-temperature arc tails. The dissociation of vibrationally excited levels of CO_2 upon collision with O atoms is the most important CO_2 conversion process.

The external magnetic field helps to reduce the gas temperature. However, the gas temperature is still too high for overpopulation the CO_2 vibrational levels, i.e., around 3300 K for an arc current of 200 mA and a magnetic field

of 0.1 T. The external magnetic field enhances the CO_2 conversion by increasing the fraction of gas treated by the arc, rather than by enhancing the vibrational-translational non-equilibrium and thus changing the dominant chemical reactions. The experimental results of a GA with and without magnetic field also support the potential of the MGA for further enhancing reactor performance.

Acknowledgements

The authors acknowledge financial support from the Fund for Scientific Research − Flanders (FWO; Grant G.0383.16N), National Natural Science Foundation of China under Grant Nos. 51706204, 51707144, and State Key Laboratory of Electrical Insulation and Power Equipment (EIPE19302). The calculations were performed using the Turing HPC infrastructure at the CalcUA core facility of Universiteit Antwerpen, a division of the Flemish Supercomputer Center VSC, funded by the Hercules Foundation, the Flemish Government (department EWI), and Universiteit Antwerpen. Finally, Hantian Zhang acknowledges financial support from the China Scholarship Council.

Appendix

Table A.1 Chemical reactions for the MGA models in argon

Reaction	Rate coefficient
$e + Ar \rightarrow e + Ar$	[a] Boltzmann solver
$e + Ar \rightarrow e + Ar(4s)$	[a] Boltzmann solver
$e + Ar \rightarrow 2e + Ar^+$	[a] Boltzmann solver
$e + Ar(4s) \rightarrow 2e + Ar^+$	[a] Boltzmann solver
$e + Ar(4s) \rightarrow e + Ar$	[a] Boltzmann solver, detailed balance
$2e + Ar^+ \rightarrow e + Ar$	$8.75 \times 10^{-39} T_e^{-2.25}(eV)$
$e + Ar + Ar^+ \rightarrow 2Ar$	$1.5 \times 10^{-40}(T_g(K)/300)^{-2.5}$
$e + Ar_2^+ \rightarrow Ar + Ar^+ + e$	$1.11 \times 10^{-12}\exp(-(2.94-3(T_g(eV)-0.026))/T_e(eV))$
$e + Ar_2^+ \rightarrow Ar + Ar(4s)$	$1.04 \times 10^{-12}(300/T_g(K))^{0.67}(1-\exp(-418(T_g(K))/(1-0.31\exp(-418(T_g(K)))$
$Ar(4s) + Ar(4s) \rightarrow e + Ar_2^+$	$3.15 \times 10^{-16}(T_g(K)/300)^{-0.5}$
$Ar(4s) + Ar(4s) \rightarrow Ar + Ar^+ + e$	$1.62 \times 10^{-16}(T_g(K))^{0.5}$
$2Ar + Ar^+ \rightarrow Ar + Ar_2^+$	$2.5 \times 10^{-43}(T_g(K)/300)^{-1.5}$
$Ar + Ar_2^+ \rightarrow 2Ar + Ar^+$	$(6.06 \times 10^{-12}/T_e(K))\exp(-1.51 \times 10^4/T_g(K))$
$Ar(4s) \rightarrow h\nu + Ar$	[b] $g_{eff} \times 3.145 \times 10^8$
$e + Ar \rightarrow e + e + Ar^+$	[c] $2 \times 10^{-33}\exp(10.2T_e(eV))$
$e + Ar + Ar \rightarrow e + e + Ar_2^+$	[c] $1 \times 10^{-55}\exp(6.9T_e(eV))$

[a] The rate coefficients are calculated using the cross sections, based on the solution with BOLSIG+[60]. The necessary cross sections for the Ar model are from the Biagi-v7.1 database (www.lxcat.net), Program Magboltz, version 7.1 JUNE 2004.

[b] $g_{eff} = (1.15/\pi)(\lambda_{4s}/(6H))$, where λ_{4s} =105.7nm and H = 1mm.

[c] In order to reduce the calculation time, we consider the reduced set of Ar chemical reactions described in Ref [35]. In the reduced chemistry set, two additional reactions (the last two reactions in this table) were added to replace the contribution of Ar(4p) and Ar_2* . The stepwise ionization of Ar(4p) was replaced using $e + Ar \rightarrow e + e + Ar^+$. The ionization of Ar_2* ($e + Ar_2^* \rightarrow e + e + Ar_2^+$) was simplified using $e + Ar + Ar \rightarrow e + e + Ar_2^+$. The reduced reaction set was validated, because it produces almost the same plasma characteristics as the full reaction set in Ref [28].

Table A.2 Chemical reactions for the MGA in CO_2. The rate coefficients are in $m^3\ s^{-1}$ for the two-body reactions, and in $m^6\ s^{-1}$ for the three-body reactions

Process	Reaction	Rate coefficient
Elastic collision	$e + CO_2 \rightarrow e + CO_2$	[a] Boltzmann solver
Ionization	$e + CO_2 \rightarrow e + e + CO_2^+$	[a] Boltzmann solver
Dissociative attachment	$e + CO_2 \rightarrow CO + O^-$	[a] Boltzmann solver

Dissociation	$e + CO_2 \rightarrow e + CO + O$	[a] Boltzmann solver
Electronic excitation	$e + CO_2 \rightarrow e + CO_2[e]$	[a] Boltzmann solver
Vibrational excitation	$e + CO_2 \rightarrow e + CO_2[v_a\text{-}v_d]$	[a] Boltzmann solver
Vibrational excitation	$e + CO_2 \rightarrow e + CO_2[v_1\text{-}v_{21}]$	[a] Boltzmann solver
Elastic collision	$e + CO \rightarrow e + CO$	[a] Boltzmann solver
Dissociative attachment	$e + CO \rightarrow C + O^-$	[a] Boltzmann solver
Dissociation	$e + CO \rightarrow e + C + O$	[a] Boltzmann solver
Elastic collision	$e + O_2 \rightarrow e + O_2$	[a] Boltzmann solver
Ionization	$e + O_2 \rightarrow e + e + O_2^+$	[a] Boltzmann solver
Dissociative attachment	$e + O_2 \rightarrow O + O^-$	[a] Boltzmann solver
Dissociation	$e + O_2 \rightarrow e + O + O$	[a] Boltzmann solver
Attachment[b]	$e + O_2 + M \rightarrow O_2^- + M$	[a] Boltzmann solver
Vibrational excitation	$e + O_2 \rightarrow e + O_2[v_1\text{-}v_3]$	[a] Boltzmann solver
Attachment	$e + O + M \rightarrow O^- + M$	1.0×10^{-31}
Electron-ion recombination[c]	$e + CO_2^+ \rightarrow CO + O$	$2.0 \times 10^{-5}(T_e)^{-0.5}/T_g$
Electron-ion recombination	$e + CO_2^+ \rightarrow C + O_2$	$3.94 \times 10^{-7}(T_e)^{-0.4}$
Electron-ion recombination	$e + O_2^+ + M \rightarrow O_2 + M$	1.0×10^{-26}
Electron-ion recombination	$e + O_2^+ \rightarrow O + O$	$6.0 \times 10^{-7}(T_e/T_g)^{-0.5}$
Recombination	$O^- + CO_2 + M \rightarrow CO_3^- + M$	9.0×10^{-29}
Electron detachment	$O^- + CO \rightarrow CO_2 + e$	5.5×10^{-10}
Electron detachment	$CO_3^- + CO \rightarrow 2CO_2 + e$	5.0×10^{-13}
Recombination	$CO_3^- + CO_2^+ \rightarrow 2CO_2 + O$	5.0×10^{-7}
Electron detachment	$O^- + M \rightarrow e + O + M$	4.0×10^{-12}
Electron detachment	$O^- + O \rightarrow e + O_2$	2.3×10^{-10}
Charge transfer	$O_2^- + O \rightarrow O^- + O_2$	3.3×10^{-10}
Electron detachment	$O_2^- + O_2 \rightarrow e + O_2 + O_2$	2.18×10^{-18}
Electron detachment	$O_2^- + M \rightarrow e + O_2 + M$	$2.7 \times 10^{-10}(T_g/300)^{0.5}\exp(-5590/T_g)$
Charge transfer	$O + CO_3^- \rightarrow CO_2 + O_2^-$	8×10^{-11}
Recombination	$O_2^- + O_2^+ \rightarrow CO + O_2 + O$	6×10^{-7}
Charge transfer	$O_2 + CO_2^+ \rightarrow CO_2 + O_2^+$	5.3×10^{-11}
Charge transfer	$O + CO_2^+ \rightarrow CO + O_2^+$	1.64×10^{-10}
Recombination	$O_2^+ + CO_3^- \rightarrow CO_2 + O_2 + O$	3×10^{-7}
Recombination	$O_2^+ + O_2^- \rightarrow O_2 + O_2$	2×10^{-7}
Recombination	$O_2^+ + O_2^- \rightarrow O_2 + O + O$	4.2×10^{-7}
Recombination	$O_2^+ + O_2^- + M \rightarrow O_2 + O_2 + M$	2×10^{-25}
Recombination	$O_2^+ + O^- \rightarrow O_2 + O$	1×10^{-7}
Recombination	$O_2^+ + O_2^- \rightarrow O_2 + O + O$	2.6×10^{-8}
Neutral reaction	$CO_2 + M \rightarrow CO + O + M$	$4.39 \times 10^{-7}\exp(-65000/T_g)$
Neutral reaction	$CO_2 + O \rightarrow CO + O_2$	$7.77 \times 10^{-12}\exp(-16600/T_g)$
Neutral reaction	$CO + O + M \rightarrow CO_2 + M$	$8.2 \times 10^{-34}\exp(-1560/T_g)$
Neutral reaction	$CO + O_2 \rightarrow CO_2 + O$	$1.28 \times 10^{-12}\exp(-12800/T_g)$
Neutral reaction	$CO_2 + C \rightarrow CO + CO$	1×10^{-15}
Neutral reaction	$O_2 + C \rightarrow CO + O$	3×10^{-11}
Neutral reaction	$CO + M \rightarrow C + O + M$	$1.52 \times 10^{-4}(T_g/298)^{-3.1}\exp(-12800/T_g)$
Neutral reaction	$C + O + M \rightarrow CO + M$	$2.14 \times 10^{-29}(T_g/300)^{-3.08}\exp(-2114/T_g)$
Neutral reaction	$O + O + M \rightarrow O_2 + M$	$1.27 \times 10^{-32}(T_g/300)^{-1}\exp(-170/T_g)$
VT relaxation	$CO_2[v_a\text{-}v_d] + M \rightarrow CO_2 + M$	$7.14 \times 10^{-8}\exp(-177/T_g^{-1/3} + 451/T_g^{-2/3})$
VT relaxation (i)[d]	$CO_2[v_i] + M \rightarrow CO_2[v_{i\text{-}1,\,a}] + M$	$0.43\exp(-407/T_g^{-1/3} + 824/T_g^{-2/3})$
VT relaxation (ii)[d]	$CO_2[v_i] + M \rightarrow CO_2[v_{i\text{-}1,\,b}] + M$	$0.86\exp(-404/T_g^{-1/3} + 1096/T_g^{-2/3})$
VT relaxation (iii)[d]	$CO_2[v_i] + M \rightarrow CO_2[v_{i\text{-}1,\,c}] + M$	$1.43 \times 10^{-5}\exp(-252/T_g^{-1/3} + 685/T_g^{-2/3})$
VV' relaxation[e]	$CO_2[v_i] + CO_2 \rightarrow CO_2[v_{i\text{-}1}] + CO_2[v_x]$	$2.13 \times 10^{-5}\exp(-242/T_g^{-1/3} + 633/T_g^{-2/3})$
VV relaxation[f]	$CO_2[v_i] + CO_2[v_j] \rightarrow CO_2[v_{i\text{-}1}] + CO_2[v_{j+1}]$	$1.8 \times 10^{-11}\exp(-24.7/T_g^{-1/3} - 65.7/T_g^{-2/3})$
VT relaxation[g]	$O_2[v_i] + M \rightarrow O_2[v_{i\text{-}1}] + M$	$7.99 \times 10^{-5}\exp(-320/T_g^{-1/3} + 615/T_g^{-2/3})$

[a] The rate coefficients are calculated using the cross sections in BOLSIG+ [60]. The cross sections for the CO_2 model are from Phelps et al. [61,62], as suggested in Ref [63]. The Fridman approximation was used to obtain the excitation cross sections for the asymmetric mode vibrational levels [42].

[b] M represents any neutral species.

[c] T_e in eV and T_g in K

[d] For i = 1, these three reactions represent VT relaxation of the first asymmetric mode level of CO_2 to the a, b, c symmetric mode levels. For i > 1, these three reactions are not considered separately (no sublevels considered), and the rate coefficient is taken as the sum of (i), (ii) and (iii), leading to level $CO_2[v_{i-1}]$ [42][41].

[e] x = a, b; $i \geq 2$

[f] $0 \leq j \leq 20$; $1 \leq i \leq 21$. v_0 means the ground state of CO_2.

[g] i =1, 2, 3. v_0 means the ground state of O_2 [20].

References

[1] Snoeckx R and Bogaerts A 2017 Plasma technology – a novel solution for CO2 conversion? *Chem. Soc. Rev.* **46** 5805–63

[2] Xu S, Khalaf P I, Martin P A and Christopher Whitehead J 2018 CO2 dissociation in a packed-bed plasma reactor: Effects of operating conditions *Plasma Sources Sci. Technol.* **27** 075009

[3] Mohsenian S, Nagassou D, Bhatta S, Elahi R and Trelles J P 2019 Design and characterization of a solar-enhanced microwave plasma reactor for atmospheric pressure carbon dioxide decomposition *Plasma Sources Sci. Technol.* **28** 065001

[4] Kotov V and Koelman P M J 2019 Plug flow reactor model of the plasma chemical conversion of CO2 *Plasma Sources Sci. Technol.* **28** 095002

[5] Ma T, Wang H X, Shi Q, Li S N and Murphy A B 2018 Breakdown and current-voltage characteristics of DC micro-slit discharges in carbon dioxide *Plasma Sources Sci. Technol.* **27** 075011

[6] Li J, Zhang X, Shen J, Ran T, Chen P and Yin Y 2017 Dissociation of CO2 by thermal plasma with contracting nozzle quenching *J. CO2 Util.* **21** 72–6

[7] Fridman A, Nester S, Kennedy L A, Saveliev A and Mutaf-Yardimci O 1999 Gliding arc gas discharge *Prog. energy Combust. Sci.* **25** 211–31

[8] Tu X, Gallon H J and Whitehead J C 2011 Dynamic behavior of an atmospheric argon gliding arc plasma *IEEE Trans. Plasma Sci.* **39** 2900–1

[9] Kim S C, Lim M S and Chun Y N 2014 Reduction characteristics of carbon dioxide using a plasmatron *Plasma Chem. Plasma Process.* **34** 125–43

[10] Baba T, Takeuchi Y, Stryczewska, Henryka D and Aoqui S 2012 Study of 6 electrodes gliding arc discharge configuration [J] *Przegląd Elektrotechniczny* **88** 86–8

[11] Liu J L, Park H W, Chung W J and Park D W 2016 High-Efficient Conversion of CO2in AC-Pulsed Tornado Gliding Arc Plasma *Plasma Chem. Plasma Process.* **36** 437–49

[12] Nunnally T, Gutsol K, Rabinovich A, Fridman A, Gutsol A and Kemoun A 2011 Dissociation of CO2 in a low current gliding arc plasmatron *J. Phys. D. Appl. Phys.* **44** 274009

[13] Ramakers M, Trenchev G, Heijkers S, Wang W and Bogaerts A 2017 Gliding Arc Plasmatron: Providing an Alternative Method for Carbon Dioxide Conversion *ChemSusChem* **10** 2642–52

[14] Gangoli S P, Gutsol A F and Fridman A A 2010 A non-equilibrium plasma source: Magnetically stabilized gliding arc discharge: I. Design and diagnostics *Plasma Sources Sci. Technol.* **19** 065003

[15] Zhang H, Li L, Li X, Wang W, Yan J and Tu X 2018 Warm plasma activation of CO2 in a rotating gliding arc discharge reactor *J. CO2 Util.* **27** 472–9

[16] McNall M and Coulombe S 2018 Characterization of a rotating gliding arc in argon at atmospheric pressure *J. Phys. D. Appl. Phys.* **51** 445203

[17] Li L, Zhang H, Li X, Huang J, Kong X, Xu R and Tu X 2020 Magnetically enhanced gliding arc discharge for CO2 activation *J. CO2 Util.* **35** 28–37

[18] Sun S, Wang H-X and Bogaerts A 2019 Chemistry reduction of complex CO2 chemical kinetics: application to a gliding arc plasma *Plasma Sources Sci. Technol.* (Accepted manuscript)

[19] Wang W, Mei D, Tu X and Bogaerts A 2017 Gliding arc plasma for CO2 conversion: Better insights by a combined experimental and modelling approach *Chem. Eng. J.* **330** 11–25

[20] Wang W, Berthelot A, Kolev S, Tu X and Bogaerts A 2016 CO2 conversion in a gliding arc plasma: 1D cylindrical discharge model *Plasma Sources Sci. Technol.* **25** 065012

[21] Sun S R, Wang H X, Mei D H, Tu X and Bogaerts A 2017 CO2conversion in a gliding arc plasma: Performance improvement based on chemical reaction modeling *J. CO2 Util.* **17** 220–34

[22] Zhu F, Zhang H, Li X, Wu A, Yan J, Ni M and Tu X 2018 Arc dynamics of a pulsed DC nitrogen rotating gliding arc discharge *J. Phys. D. Appl. Phys.* **51** 105202

[23] Zhang H, Wang W, Li X, Han L, Yan M, Zhong Y and Tu X 2018 Plasma activation of methane for hydrogen production in a N 2 rotating gliding arc warm plasma: a chemical kinetics study *Chem. Eng. J.* **345** 67–78

[24] Hao Z, Fengsen Z, Xin T, Zheng B, Kefa C and Xiaodong L 2016 Characteristics of Atmospheric Pressure Rotating Gliding Arc Plasmas *Plasma Sci. Technol.* **18** 473

[25] Zhang H, Wu Y, Sun H, Yang F, Rong M, Jiang F, Wang C and Huang W 2019 Application of Calibration-Free Boltzmann Plot Method for Composition and Pressure Measurement in Argon Free-Burning Arcs *Plasma Chem. Plasma Process.* **39** 1429–47

[26] Generator S P, Namihira T, Member S, Sakai S, Yamaguchi T, Yamamoto K, Yamada C, Kiyan T and Sakugawa T 2007 Electron Temperature and Electron Density of Underwater Pulsed Discharge Plasma Produced by *IEEE Trans. Plasma Sci.* **35** 614–8

[27] Kramida A, Ralchenko Y and Reader J 2018 NIST atomic spectra database (ver. 5.6.1) *Natl. Inst. Stand. Technol. Gaithersburg, MD*

[28] Kolev S and Bogaerts A 2015 A 2D model for a gliding arc discharge *Plasma Sources Sci. Technol.* **24** 015025

[29] Trenchev G, Kolev S and Bogaerts A 2016 A 3D model of a reverse vortex flow gliding arc reactor *Plasma Sources Sci. Technol.* **25** 35014

[30] Trenchev G, Kolev S, Wang W, Ramakers M and Bogaerts A 2017 CO2 Conversion in a Gliding Arc Plasmatron: Multidimensional Modeling for Improved Efficiency *J. Phys. Chem. C* **121** 24470–9

[31] Trenchev G, Nikiforov A, Wang W, Kolev S and Bogaerts A 2019 Atmospheric pressure glow discharge for CO2 conversion: Model-based exploration of the optimum reactor configuration *Chem. Eng. J.* **362** 830–41

[32] Sun S R, Kolev S, Wang H X and Bogaerts A 2017 Investigations of discharge and post-discharge in a gliding arc: a 3D computational study *Plasma Sources Sci. Technol.* **26** 055017

[33] Zhang H, Du C, Wu A, Bo Z, Yan J and Li X 2014 Rotating gliding arc assisted methane decomposition in nitrogen for hydrogen production *Int. J. Hydrogen Energy* **39** 12620–35

[34] COMSOL Multiphysics, Version 5.4; User's Guide, 2018; www.comsol.com

[35] Sun S R, Kolev S, Wang H X and Bogaerts A 2017 Coupled gas flow-plasma model for a gliding arc: Investigations of the back-breakdown phenomenon and its effect on the gliding arc characteristics *Plasma Sources Sci. Technol.* **26** 015003

[36] Paunska T, Trenchev G, Bogaerts A and Kolev S 2019 A 2D model of a gliding arc discharge for CO2 conversion *AIP Conf. Proc.* **2075** 060008

[37] Trenchev G, Kolev S and Bogaerts A 2016 A 3D model of a reverse vortex flow gliding arc reactor *Plasma Sources Sci. Technol.* **25** 035014

[38] El-Zein A, Talaat M, El-Aragi G and El-Amawy A 2015 Experimental model to study the characteristics of gliding arc plasma reactor with argon/nitrogen *J. Electr. Eng.* **15** 64–7

[39] Sember V and Svoboda P 1993 Spectroscopic measurements of glidarc plasma chemical reactor *16th SYMPOSIUM ON PLASMA PHYSICS AND TECHNOLOGY* (Prague) p 230

[40] Berthelot A and Bogaerts A 2016 Modeling of plasma-based CO2 conversion: Lumping of the vibrational levels *Plasma Sources Sci. Technol.* **25** 045022

[41] Kozák T and Bogaerts A 2015 Evaluation of the energy efficiency of CO2 conversion in microwave discharges using a reaction kinetics model *Plasma Sources Sci. Technol.* **24** 015024

[42] Kozàk T and Bogaerts A 2014 Splitting of CO2 by vibrational excitation in non-equilibrium plasmas: A reaction kinetics model *Plasma Sources Sci. Technol.* **23** 045004

[43] Levine R D and Bernstein R B 1976 Thermodynamic approach to collision processes *Dynamics of Molecular Collisions* (Springer) pp 323–64

[44] Fridman A 2008 *Plasma chemistry* (Cambridge university press)

[45] Sun Z W, Zhu J J, Li Z S, Aldén M, Leipold F, Salewski M and Kusano Y 2013 Optical diagnostics of a gliding arc *Opt. Express* **21** 6028

[46] Zhu J, Gao J, Ehn A, Aldén M, Li Z, Moseev D, Kusano Y, Salewski M, Alpers A and Gritzmann P 2015 Measurements of 3D slip velocities and plasma column lengths of a gliding arc discharge *Appl. Phys. Lett.* **106** 44101

[47] Wu A J, Zhang H, Li X D, Lu S Y, Du C M and Yan J H 2014 Spectroscopic diagnostics of rotating gliding arc plasma codriven by a magnetic field and tangential flow *IEEE Trans. Plasma Sci.* **42** 3560–8

[48] Richard F, Cormier J M, Pellerin S and Chapelle J 1996 Physical study of a gliding arc discharge *J. Appl. Phys.* **79** 2245–50

[49] Kolev S and Bogaerts A 2018 Three-dimensional modeling of energy transport in a gliding arc discharge in argon *Plasma Sources Sci. Technol.* **27** 125011

[50] Li L, Zhang H, Li X, Kong X, Xu R, Tay K and Tu X 2019 Plasma-assisted CO2 conversion in a gliding arc discharge: Improving performance by optimizing the reactor design *J. CO2 Util.* **29** 296–303

[51] Indarto A, Choi J-W, Lee H and Song H K 2006 Conversion of CO2 by Gliding Arc Plasma *Environ. Eng. Sci.* **23** 1033–43

[52] Yang G and Heberlein J V 2007 The anode region of high intensity arcs with cold cross flow *J. Phys. D. Appl. Phys.* **40** 5649

[53] Trelles J P, Chazelas C, Vardelle A and Heberlein J V R 2009 Arc plasma torch modeling *J. Therm. spray Technol.* **18** 728–52

[54] Berthelot A and Bogaerts A 2017 Modeling of CO 2 Splitting in a Microwave Plasma: How to Improve the Conversion and Energy Efficiency *J. Phys. Chem. C* **121** 8236–51

[55] Kim S C and Chun Y N 2014 Development of a gliding arc plasma reactor for CO2 destruction *Environ. Technol. (United Kingdom)* **35** 2940–6

[56] Taylan O and Berberoglu H 2015 Dissociation of carbon dioxide using a microhollow cathode discharge plasma reactor: Effects of applied voltage, flow rate and concentration *Plasma Sources Sci. Technol.* **24** 015006

[57] Xu S, Whitehead J C and Martin P A 2017 CO2 conversion in a non-thermal, barium titanate packed bed plasma reactor: The effect of dilution by Ar and N2 *Chem. Eng. J.* **327** 764–73

[58] Ramakers M, Michielsen I, Aerts R, Meynen V and Bogaerts A 2015 Effect of argon or helium on the CO2 conversion in a dielectric barrier discharge *Plasma Process. Polym.* **12** 755–63

[59] Nunnally T P 2011 *Application of low current gliding arc plasma discharges for hydrogen sulfide decomposition and carbon dioxide emission reduction* (Drexel University)

[60] Hagelaar G J M and Pitchford L C 2005 Solving the Boltzmann equation to obtain electron transport coefficients and rate coefficients for fluid models *Plasma Sources Sci. Technol.* **14** 722

[61] Lowke J J, Phelps A V. and Irwin B W 1973 Predicted electron transport coefficients and operating characteristics of CO2-N2-He laser mixtures *J. Appl. Phys.* **44** 4664–71

[62] Hake Jr R D and Phelps A V 1967 Momentum-Transfer and Inelastic-Collision Cross Sections for Electrons in O2, CO, and CO2 *Phys. Rev.* **158** 70

[63] Bogaerts A, Wang W, Berthelot A and Guerra V 2016 Modeling plasma-based CO2 conversion: Crucial role of the dissociation cross section *Plasma Sources Sci. Technol.* **25** 055016